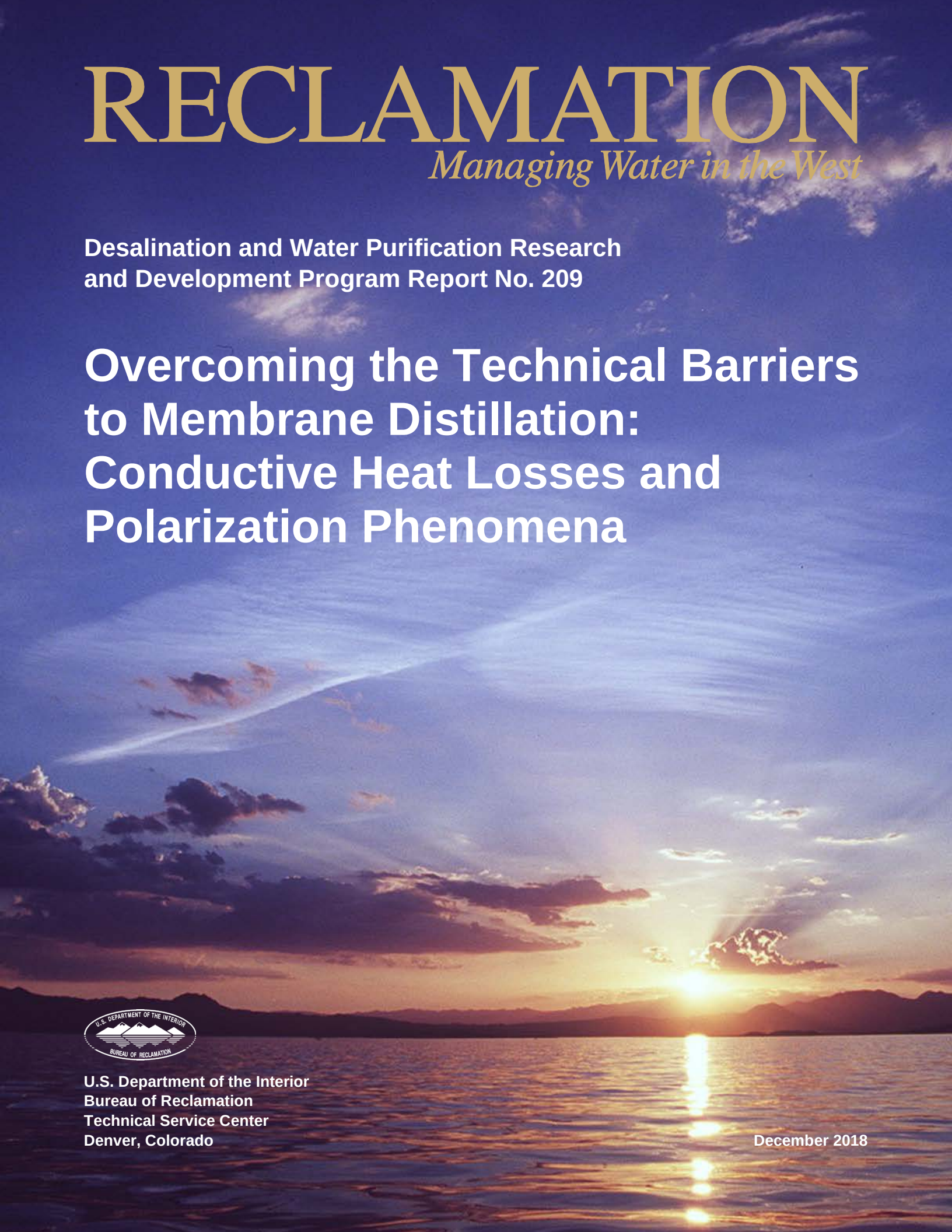

RECLAMATION

Managing Water in the West

Desalination and Water Purification Research and Development Program Report No. 209

Overcoming the Technical Barriers to Membrane Distillation: Conductive Heat Losses and Polarization Phenomena

U.S. Department of the Interior
Bureau of Reclamation
Technical Service Center
Denver, Colorado

December 2018

This page intentionally left blank.

REPORT DOCUMENTATION PAGE		Form Approved OMB No. 0704-0188

1. REPORT DATE *(DD-MM-YYYY)*	2. REPORT TYPE	3. DATES COVERED *(From - To)*
12/30/2018	Final	9/1/2016-12/30/2018

4. TITLE AND SUBTITLE	5a. CONTRACT NUMBER
Overcoming the Technical Barriers to Membrane Distillation: Conductive Heat Losses and Polarization Phenomena. Final Report	Agreement No. R16AC00121
	5b. GRANT NUMBER
	5c. PROGRAM ELEMENT NUMBER
6. AUTHOR(S) Dr. Nils Tilton, Assistant Professor of Mechanical Engineering Dr. Steven DeCaluwe, Assistant Professor of Mechanical Engineering	5d. PROJECT NUMBER
	5e. TASK NUMBER
	5f. WORK UNIT NUMBER

7. PERFORMING ORGANIZATION NAME(S) AND ADDRESS(ES)	8. PERFORMING ORGANIZATION REPORT NUMBER
Colorado School of Mines 1500 Illinois Street Golden, CO 80401	
9. SPONSORING/MONITORING AGENCY NAME(S) AND ADDRESS(ES)	10. SPONSOR/MONITOR'S ACRONYM(S)
Bureau of Reclamation U.S. Department of the Interior Denver Federal Center PO Box 25007, Denver, CO 80225-0007	Reclamation
	11. SPONSOR/MONITOR'S REPORT NUMBER(S) DWPR Report No. 209

12. DISTRIBUTION/AVAILABILITY STATEMENT
Available from the National Technical Information Service, Operations Division, 5285 Port Royal Road, Springfield VA 22161

13. SUPPLEMENTARY NOTES
Online at https://www.usbr.gov/research/dwpr/DWPR_Reports.html

14. ABSTRACT

DCMD efficiency is determined by a complex interplay between transport in the feed, membrane, and permeate. We explored this interplay using pore-scale analysis, bench-scale experiments and CFD. We first compared the bench-scale performance of 17 potential DCMD membranes from six vendors. No clear trend appeared to consistently explain why one membrane outperformed another. We then pioneered the use of FIB-SEM for accurate 3D reconstruction of porous membrane microstructures. For that purpose, we developed protocols for membrane infiltration by staining membranes with heavy-metal salts and by incorporating conductive polymers into the epoxy. We nevertheless found that FIB-SEM was unable to resolve the nanometer-scale fibers within membranes. We consequently explored other methods of simulating pore-scale transport. Our results suggest that simple Fickian models of molecular diffusion and pressure-driven Darcy flow may accurately predict trans-membrane fluxes.

We then developed an in-house CFD code that simulates heat and mass transport in 2D DCMD systems. The code was validated against dedicated experiments and used to study temperature polarization, concentration polarization, and system-level efficiency as a function of operating conditions and co- vs. counter-current operation. We showed that common Nusselt and Sherwood number relationships do not accurately predict temperature and concentration polarization. Moreover, though DCMD systems have small vapor fluxes, they produce significant concentration polarization. Compounding effects of temperature and concentration polarization can also have counter-intuitive

<table>
<tr><td colspan="6">effects on local transmembrane vapor flux, such that the maximum vapor flux does not occur where the transmembrane temperature is maximized. Furthermore, counter-current operation was found to only produce a marginal increase in net vapor production but has a significantly greater concentration polarization. As a result, co-current systems were found to have a higher Gained Output Ratio than counter-current systems.</td></tr>
<tr><td colspan="6">15. SUBJECT TERMS</td></tr>
<tr><td colspan="3">16. SECURITY CLASSIFICATION OF:</td><td>17. LIMITATION OF ABSTRACT</td><td>18. NUMBER OF PAGES</td><td>19a. NAME OF RESPONSIBLE PERSON
Katie Guerra</td></tr>
<tr><td>a. REPORT
U</td><td>b. ABSTRACT
U</td><td>THIS PAGE
U</td><td></td><td></td><td>19b. TELEPHONE NUMBER (Include area code)
303-445-2013</td></tr>
</table>

Desalination and Water Purification Research and Development Program Report No. 209

Overcoming the Technical Barriers to Membrane Distillation: Conductive Heat Losses and Polarization Phenomena

Prepared for the Bureau of Reclamation Under Agreement No. R16AC00121

by

Nils Tilton and Steven DeCaluwe

Colorado School of Mines

Request for Proposal No. 05SF811067

Mission Statements

The U.S. Department of the Interior protects America's natural resources and heritage, honors our cultures and tribal communities, and supplies the energy to power our future.

The mission of the Bureau of Reclamation is to manage, develop, and protect water and related resources in an environmentally and economically sound manner in the interest of the American public.

Disclaimer

The views, analysis, recommendations, and conclusions in this report are those of the authors and do not represent official or unofficial policies or opinions of the United States Government, and the United States takes no position with regard to any findings, conclusions, or recommendations made. As such, mention of trade names or commercial products does not constitute their endorsement by the United States Government.

Acknowledgments

This work was generously funded by the Bureau of Reclamation Desalination and Water Purification Research and Development Program.

- **Nils Tilton:** Dr. Tilton is an assistant professor in the Department of Mechanical Engineering. He led the CFD efforts and coordinated collaboration between the co-investigators.
- **Steven DeCaluwe:** Dr. DeCaluwe is an assistant professor in the Department of Mechanical Engineering. He supervised the pore-scale FIB-SEM and transport modeling.
- **Johan Vanneste:** Dr. Vanneste is an assistant research professor in the Department of Civil and Environmental Engineering. He supervised the bench-scale characterization of membranes.
- **Tzahi Cath:** Dr. Cath is a full professor in the Department of Civil and Environmental Engineering and the director of the Advanced Water Technology Center (AQWATEC). He aided in the interpretation of data and outreach to membrane manufacturers.
- **Christopher Bellona:** Dr. Bellona is an assistant professor in the Department of Civil and Environmental Engineering. He assisted in the processing and interpretation of the bench-scale data.

Acronyms and Abbreviations

1D	one-dimensional
2D	two-dimensional
3D	three-dimensional
AQWATEC	Advanced Water Technology Center
CFD	computational fluid dynamics
CSM	Colorado School of Mines
DCMD	direct contact membrane distillation
DGM	Dusty Gas Model
ECTFE	ethylene chlorotrifluoroethylene
ePTFE	elongated polytetrafluoroethylene
FIB-SEM	focused ion beam - scanning electron microscopy
GOR	gained output ratio
GUI	graphic user interface
MD	membrane distillation
PE	polyester
PP	polypropylene
PVDF	polyvinylidene difluoride
Reclamation	Bureau of Reclamation
ROI	region of interest
SSR	squared residuals

Measurements

°C	degree Celsius
cm	centimeter
cm^2	square centimeters
cm/s	centimeters per second
cP	centipoise (10^{-3} Pa·s)
g	gram
g/l	grams per liter
kg	kilogram
kV	kilovolt
L/min	liters per minute
L	liter
LMH	liters per square meter per hour
mm	millimeter
mL	milliliter
mol	mole
m/s	meters per second
nA	nanoampere
nm	nanometer
Pa	Pascal
$W/(m^2K)$	Watts per square meter per Kelvin
µm	micron

Contents

Figures

Tables

This page intentionally left blank.

Executive Summary

This project explored the application of direct-contact membrane distillation (DCMD) to desalinating high-concentration brines. The work explored three key technological barriers that must be solved for DCMD to receive wide industrial application.

- **Conductive heat losses**: Currently, DCMD systems lose up to 85 percent of their feed energy to heat conduction through the membrane (Vanneste et. al 2018). These losses depend on complicated membrane pore structures that are poorly understood.
- **Temperature and Concentration Polarization:** When treating high-concentration brines with DCMD, temperature and concentration polarization reduce the vapor flux through the membrane and produce mineral scaling that damages membranes and leads to pore wetting. To date, polarization has proven exceedingly difficult to observe directly through experiments. Rather, experiments typically only measure inlet and outlet data and observe concentration polarization indirectly by studying mineral scale formation. Numerical modeling should consequently play a critical role in simulating polarization and enabling the design of DCMD systems that minimize polarization.

Thus, this project had two primary objectives.

1. **Determine design criteria for developing new membranes via pore-scale modeling of heat and vapor transport.** To explore how membrane pore-structures influence heat and vapor transport across the membrane, we explored using focused ion beam scanning electron microscopy (FIB-SEM) to directly measure three-dimensional (3D) membrane pore structures. To understand how pore-structures influence membrane performance, our objective was to numerically reconstruct the pore structures of membranes currently used in DCMD systems and then perform pore-scale simulations of heat and vapor transport. These simulations would also inform the development of new continuum-level models for coupling with bench-scale computational fluid dynamics (CFD) described in Objective 2 below. We found, however, that FIB-SEM was unable to resolve the nanometer-scale fibers within membranes. We consequently explored other methods of simulating pore-scale transport. Our results suggest that simple Fickian models of molecular diffusion and pressure-driven Darcy flow may accurately predict trans-membrane fluxes.
2. **Determine how fluid mixing can minimize temperature and concentration polarization.** We performed CFD simulations of solute

transport and heat transfer in bench-scale DCMD plate-and-frame systems using computer codes developed at the Colorado School of Mines (CSM). Simulations of DCMD are challenging because it is not computationally feasible to explicitly include pore-scale transport. Rather, the feed and permeate regions must be coupled with effective boundary conditions that model transmembrane transport. Our objective was to use the results from Objective 1 to develop improved coupling between CFD feed/permeate simulations and pore-scale transport models. Simulations provided the full velocity, temperature, and concentration fields, from which we determined the coupling between fluid mechanics and polarization. Simulations were validated with experimental bench-scale measurements.

Study results included:

- **Bench-scale membrane characterization:** In this study, we compared the bench-scale performance of 17 potential DCMD membranes from six vendors. The membranes covered every active later material commonly considered for DCMD, and encompassed a wide range of porosities, thicknesses, and supporting layers. The large spread in membrane properties yielded a large spread in vapor flux, thermal efficiency, rejection, and contact angle. Overall, we observed that membranes without support layers, higher porosities, and smaller thicknesses tended to have greater vapor flux; however, there were important exceptions. Thus, no clear trend appeared to consistently explain why one membrane outperforms another. Thus motivated, we selected five membranes for pore-scale analysis using FIB-SEM.
- **Pore-scale FIB-SEM:** Our study pioneered the 3D reconstruction of porous membrane microstructures using FIB-SEM. Such microstructures are key in controlling the permeate water flux and conductive heat loss rates. Bench-scale membrane testing demonstrates varying performance for membranes with nominally similar microstructures. Understanding such counter-intuitive results requires better characterization of membrane microstructures and improved mechanistic understanding of how these microstructures influence trans-membrane heat and mass transfer.

  In this study, we demonstrate the first-ever use of FIB-SEM for microstructural characterization of MD membranes. Sample preparation presents a key difficulty in performing this analysis, particularly providing significant electrical conductivity and electron microscope contrast between the epoxy used to fill membrane pores and the solid membrane polymer. We demonstrate protocols for membrane infiltration via membrane staining with heavy metal salts and via incorporating conductive polymers into the epoxy. While the resulting FIB-SEM images do not fully resolve the membrane microstructure (in particular, the thin,

nanometer-scale fibers connecting larger clusters of fibers are not resolved via the FIB-SEM images), these images provide an initial view into the complex membrane microstructures and demonstrate the bimodal nature of the polymer structure, which consists of finer (roughly 40 to 50 nanometers [nm] thick) fibers that connect larger bundles. Moreover, with the sample preparation protocols established in this study, future work can focus on optimizing the FIB-SEM imaging conditions for fully resolved 3D microstructures.

- **Pore-scale transport simulations:** Detailed one-dimensional (1D) pore-scale transport models were validated against the aforementioned bench-scale DCMD experiments to understand the influence of membrane microstructure on membrane performance and its coupling with operating conditions (such as feed and permeate temperatures).

  Fitting against the experimental data here leads to several important conclusions:

  1) The tortuosity factor plays a critical role in describing the impact of microstructure on membrane distillation (MD) fluxes.

  2) Moreover, the fitted tortuosity factors are influenced not only by the microstructure but also vary with operating conditions such as temperature.

  3) Finally, results show that typical theories that underpin porous media transport models are not directly transferrable to MD. In particular, while the commonly used Knudsen number would predict that molecular diffusion and Knudsen diffusion both play important roles in pore-scale MD transport processes, results here suggest that the effects of Knudsen diffusion are rather limited. Instead, results suggest that simpler, Fickian models of molecular diffusion with pressure-driven Darcy flow more accurately predict trans-membrane fluxes.

- **Bench-scale CFD:** We developed an in-house CFD code that simulates heat and mass transport in two-dimensional (2D) DCMD systems. The code was developed using well-established models for transmembrane heat and mass transport, and was validated against dedicated experiments in a bench-scale DCMD system. The code was then used to perform a comprehensive parametric study of temperature polarization, concentration polarization, and system-level efficiency as a function of co- vs. counter-current operation, operating temperature, feed concentration, flow rate, and system length.

Our CFD study showed that common Nusselt (Hausen 1943) and Sherwood number (De and Bhattacharya 1997) relationships do not accurately predict temperature and concentration polarization. Moreover, though DCMD systems have small vapor fluxes, they produce significant concentration polarization. Compounding effects of temperature and concentration polarization can also have counter-intuitive effects on local transmembrane vapor flux, such that the maximum vapor flux does not occur where the transmembrane temperature is maximized. Furthermore, counter-current operation marginally increased net vapor production but showed a significantly greater concentration polarization. As a result, co-current systems were found to have a higher Gained Output Ratio than counter-current systems.

1. Introduction

1.1. Project Background

This project was motivated by the Bureau of Reclamation (Reclamation)'s 2016 priorities of minimizing concentrate volume and developing improved membranes and desalination methods for potable reuse. Specifically, we focused on direct contact membrane distillation (DCMD), which is an emerging approach to desalinating high-concentration brines, brackish waters, produced waters, and seawater. Though attracting considerable attention, several technological barriers must be solved for DCMD to see wide industrial application. We explored these barriers using a holistic approach that combined three-dimensional (3D) microscopic imaging, numerical simulations, and bench-scale experiments.

DCMD is a thermal process in which warm feed and cool permeate flow on opposite sides of a hydrophobic membrane, as in Figure 1. The temperature difference across the membrane causes water to evaporate from the feed, travel through the membrane pores, and condense in the permeate. This has numerous advantages over reverse osmosis. DCMD can treat high concentration brines because:

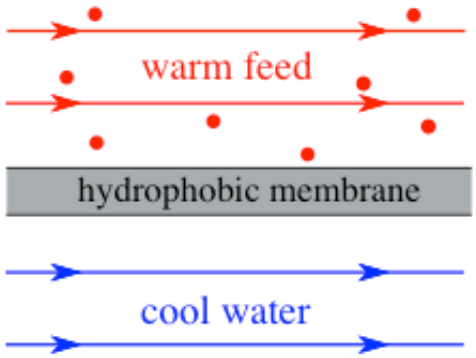

Figure 1. Direct contact membrane distillation.

- Its operation is less sensitive to osmotic pressure than reverse osmosis while offering the same level of salt rejection. While reverse osmosis is only practical for NaCl solutions up to 40 grams per liter (g/l), the limit for DCMD is around 300 g/l.
- DCMD systems do not require a pressure difference across the membrane, do not require high-pressure pumps, and can be built with inexpensive plastics, with lower capital costs.
- DCMD systems operate at feed temperatures between 40 and 90 degrees Celsius (°C) that are readily produced by industrial waste heat or solar and geothermal energy.

1.2. Project Needs and Objectives

1.2.1. Needs

This project explored three key technological challenges related to heat and mass transport occurring in the membrane, feed flow, and permeate flow:

- **Conductive heat loss:** Preliminary experiments showed that current DCMD systems lose between 45 and 85 percent of their feed energy to heat conduction through the membrane (Vanneste et al. 2018). Though previous work funded by DWPR (Sirkar and Qin 2001 and Sirkir and Song 2009) has recommended developing new low-conductivity membranes, these heat losses ultimately depend on complicated membrane pore structures that are poorly understood.
- **Temperature and concentration polarization:** *Temperature polarization* represents a reduction in the transmembrane temperature difference due to heat transfer through the membrane. *Concentration polarization* describes the accumulation of solutes adjacent to the feed side of the membrane. Both polarization phenomena reduce the vapor flux through the membrane, and a recent study concluded that they are the most crucial phenomena affecting MD treatment of hyper-saline brines (Bouchrit et al. 2015). Concentration polarization is also responsible for mineral scaling that can damage the membrane and lead to pore wetting. Numerous studies, including DWPR-funded work (Sirkar and Qin 2001, Sirkar 2003, and Sirkar and Song 2009), recommend designing DCMD systems to optimize fluid mixing and to mitigate polarization. To date, polarization has proven exceedingly difficult to observe directly through experiments. Rather, experiments typically only measure inlet and outlet data, and observe concentration polarization indirectly by studying mineral scale formation. Numerical modeling should play a critical role in elucidating polarization and enabling the design process. However, accurate simulations are inhibited by the incomplete understanding of the fluid mechanics of DCMD and the membrane transport processes to which they are coupled.

1.2.2. Objectives

DCMD efficiency is determined by a complex interplay between transport in the feed, membrane, and permeate. We explored this interplay with a holistic approach that combined pore-scale analysis, bench-scale experiments, and CFD.

- **Objective 1:** Our first objective was to determine design criteria for the development of new membranes via predictive pore-scale modeling of heat and vapor transport. To date, membrane transport models have struggled to predict the influence of microstructure due to poor representation of membrane pore-structures (Schofield et al. 1987, Lawson and Lloyd 1997, Khayet et al. 2010, Khayet 2011, Andrjesdóttir et al 2013, Field et al. 2013, Rao et al 2014, Hitsov et al. 2015, and Shirazi et al. 2016). Existing models consider ideal pores, as sketched in Figure 2, whereas actual membranes have complicated pores that vary with material and manufacturing. Consequently, different membranes produce significantly different vapor fluxes and heat losses in ways that are difficult to predict or explain. To understand how pore-structure influences transport, we explored using focused ion beam scanning electron microscopy (FIB-SEM) to directly measure 3D membrane pore structures. Using the FIB-SEM data, we numerically reconstructed the pore structures. Our objective was to then perform 3D pore-scale simulations of heat and vapor transport. Simulation results would then inform the development of new continuum-level models for coupling with CFD in Objective 2.

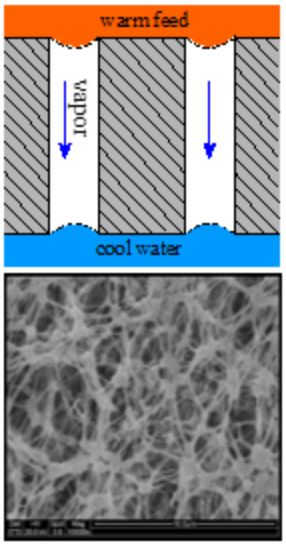

Figure 2. Ideal vs. actual pore structures

- **Objective 2:** Our second objective was to determine how fluid mixing can minimize polarization. We performed fluid dynamics (CFD) simulations of solute transport and heat transfer in bench-scale DCMD systems using codes developed at the Colorado School of Mines (CSM). CFD simulations of DCMD are challenging because it is not computationally feasible to explicitly include pore-scale transport. Rather, the feed and permeate regions must be coupled by effective boundary conditions that model transmembrane transport. Our objective was to use the results from Objective 1 to develop improved coupling between CFD feed/permeate simulations and pore-scale transport models. Simulations provide the full velocity, temperature, and concentration fields from which we determined the coupling between fluid mechanics and polarization. Simulations were validated with experimental bench-scale measurements.

1.3. Project Overview

1.3.1. Overall Methods and Concepts

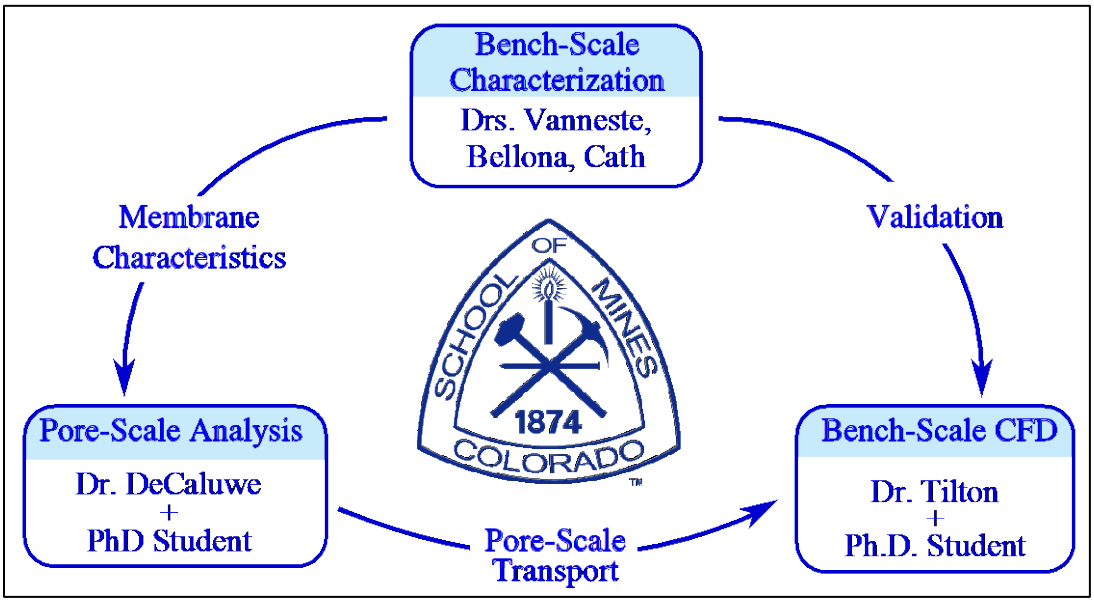

Figure 3. Project methods and management.

The project methods and management are summarized in the flow chart displayed in Figure 3. Bench-scale measurements were performed at CSM's Advanced Water Technology Center (AQWATEC) to characterize and compare the performance of 17 different DCMD membranes. We identified five membranes with widely varying performance, from good to bad, for further pore-scale analysis. Simultaneously, to explore how different pore-structures influence the bench-scale membrane performance, we developed FIB-SEM procedures to measure the 3D pore-structures of these selected membranes. To our knowledge, ours was the first study to attempt FIB-SEM measurement of DCMD membranes. In practice, developing appropriate FIB-SEM procedures proved extremely challenging. Though we made considerable progress toward measuring DCMD membrane pore-structures, we were unable to successfully compare the pore structures of the five selected membranes. Further details are provided in Section 2.2.

In parallel to the bench-scale membrane characterization and pore-scale FIB-SEM analysis, a team led by Dr. Nils Tilton developed an in-house CFD code to perform high-accuracy numerical simulations of fluid flow, heat transport, and mass transport within bench-scale DCMD plate-and-frame systems. Coupling the transport within the feed and distillate channels proved challenging, particularly near the channel inlets and outlets where transmembrane phenomena produce unique difficulties that are not discussed in the CFD literature. Further details are provided in Section 2.4. These challenges were overcome, and we successfully

validated the CFD code with bench-scale measurements performed at AQWATEC. We then performed a two-dimensional (2D) parametric study of temperature and concentration polarization in DCMD systems. We also developed a 3D version of the CFD code to allow ongoing analysis of three-dimensional polarization.

1.3.2. Participants

- **Nils Tilton:** Dr. Tilton is an assistant professor in the Department of Mechanical Engineering. He led the CFD efforts and coordinated collaboration between the co-investigators.
- **Steven DeCaluwe:** Dr. DeCaluwe is an assistant professor in the Department of Mechanical Engineering. He supervised the pore-scale FIB-SEM and transport modeling.
- **Johan Vanneste:** Dr. Vanneste is an assistant research professor in the Department of Civil and Environmental Engineering. He supervised the bench-scale characterization of membranes.
- **Tzahi Cath:** Dr. Cath is a full professor in the Department of Civil and Environmental Engineering and the director of the Advanced Water Technology Center (AQWATEC). He aided in the interpretation of data and outreach to membrane manufacturers.
- **Christopher Bellona:** Dr. Bellona is an assistant professor in the Department of Civil and Environmental Engineering. He assisted in the processing and interpretation of the bench-scale data.

2. Technical Approach and Methods

2.1. Bench-Scale Experiments

For the bench-scale characterization of DCMD membranes, we obtained 17 hydrophobic, microporous membranes from the six vendors listed in Table 2. Of these, Aquastill and CLARCOR membranes were the only membranes specifically fabricated for DCMD. For each membrane, we measured the membrane flux, thermal efficiency, rejection, and contact angle. Table 1 summarizes the membrane materials and properties reported by the manufacturers. Every active layer material commonly considered for DCMD is represented. Pore sizes range from 0.05 to 0.79 microns (μm), thicknesses range from 25 to 305 μm, and porosity ranges from 41 to 85 percent. The 17 membranes were tested in a modified acrylic SEPA flow cell having a membrane area of 136 square centimeters (cm^2) and flow channel dimensions of 145 millimeters (mm)

long, 94 mm wide, and 2.5 mm deep. Additional description is given in Bush et al. (2016). The same diamond spacer was used in the feed and distillate channel. It had a hydrodynamic angle of 70 degrees, a filament diameter of 2.3 mm, and a mesh width of 10.8 mm. Inlet and outlet temperatures on feed and distillate channels were measured, as well as flux through volume change in the distillate tank.

Table 1. Membrane Characteristics Provided by the Manufacturers

Manufacturer	Model Number	Active layer	Support Material	Nominal Pore Size (μm)	Thickness (μm)	Porosity (%)
3M	0.2 micron	PP	No	0.59 [2]	110	85
	0.45 micron	PP	No	0.79 [2]	110	85
	ECTFE	ECTFE	No	0.43 [2]	46	67
Aquastill	0.3 micron	PVDF	No	0.3	76	85
Celgard	2400	PP	No	0.043	25	41
	2500	PP	No	0.064	25	55
CLARCOR	QL218	ePTFE	PP	0.45	254-305	70-85 [1]
	QL822	ePTFE	PP	0.45	127-203	70-85 [1]
	QP952	ePTFE	PE	0.45	150-300	70-85 [1]
	QP955	ePTFE	PE	0.1	127-305	70-85 [1]
	QP961	Oleophobic ePTFE	PE	0.05	76-203	70-85 [1]
	QM902	ePTFE	No	0.45	90	70-85 [1]
Osmonics Corp.	PP22	PP	No	0.22	150	70
	TS22	PTFE	PP	0.22	175	70
	PVDF	PVDF	No	0.4	160	-
Pall Corp.	0.2 micron	PTFE	LDA[3]	0.2	179-246	-

Manufacturer	Model Number	Active layer	Support Material	Nominal Pore Size (µm)	Thickness (µm)	Porosity (%)
	0.45 micron	PTFE	LDA[3]	0.45	191-257	-

Shaded membranes were selected for further characterization in this study.

PP = polypropylene

ECTFE = ethylene chlorotrifluoroethylene

PVDF = polyvinylidene difluoride

ePTFE = elongated polytetrafluoroethylene

PE = polyester

[1] Manufacturer's estimate

[2] Bubble point pore diameter

[3] Non-woven polypropylene

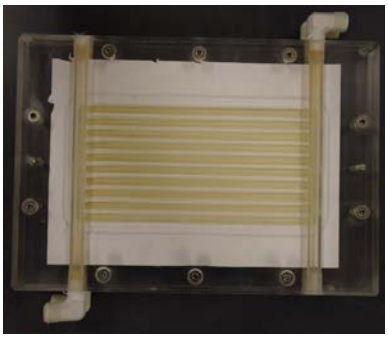

Figure 4. Ten-channel flow cell

In addition to the membrane characterization, bench-scale experiments were performed to measure the membrane thermal conductivity and vapor permeability required for our bench-scale CFD simulations. Details of their measurement are provided in section 2.4.2. Because currently we cannot perform CFD simulations with spacers, we developed another acrylic flow cell with 10 feed and distillate channels machined into acrylic plates that can be operated without a spacer, as shown in Figure 4. Additional description is given in Bush et al. (2016). The 10 channels have identical dimensions: 17.78 centimeters (cm) long, 3.175 mm high, and 6.35 mm wide. The relatively small width is required to minimize membrane warping.

2.2. Pore-Scale Microscopy

The microstructural characterization uses FIB-SEM to characterize MD membrane microstructures. FIB-SEM combines 2D SEM imaging with a focused ion beam used to mill away material (Smith et al. 2009, Sears et al. 2010, and Wiedemann et al. 2013). The 3D structure is obtained by taking a 2D SEM image, milling away a thin layer of material, taking a new image, and repeating. The series of 2D images are digitally combined to reconstruct the full 3D structure, which is then analyzed to determine microstructural parameters such as porosity,

tortuosity, and mean pore diameter. The process is illustrated in Figure 5, which shows the reconstruction of a nanocomposite polymer (Sheidaei 2013). The technique provides high-resolution, detailed, accurate microstructural information. This technique has been successfully applied to a range of porous materials (Smith et al. 2009, Sears et al. 2010, Wiedemann et al. 2013).

The primary challenge of the FIB-SEM measurements in this study relates to the infiltration protocol. In this process, pores in the sample are entirely filled with a material that provides high SEM contrast with the polymer material. Infiltration with epoxy is required for an unambiguous picture of the 3D microstructure, for two primary reasons:

1. Due to the high degree of open porosity, the epoxy fills the open pores in the resulting SEM images, so that multiple layers of polymer material do not appear in a single SEM "slice" image. The epoxy therefore disambiguates membrane materials at different depths.
2. Due to the low electronic conductivity of the polymer membrane, an epoxy with an added conductive component is needed to prevent "curtaining" (i.e., distortion) of the resulting SEM images and to provide material stability under both the electron and ion beams of the FIB-SEM device. Failure to attain complete infiltration with a conductive epoxy resin can lead to sample damage under beam conditions and/or inability to perform the slice-and-view procedure. Both inhibit proper FIB-SEM analysis for creating 3D reconstructions.

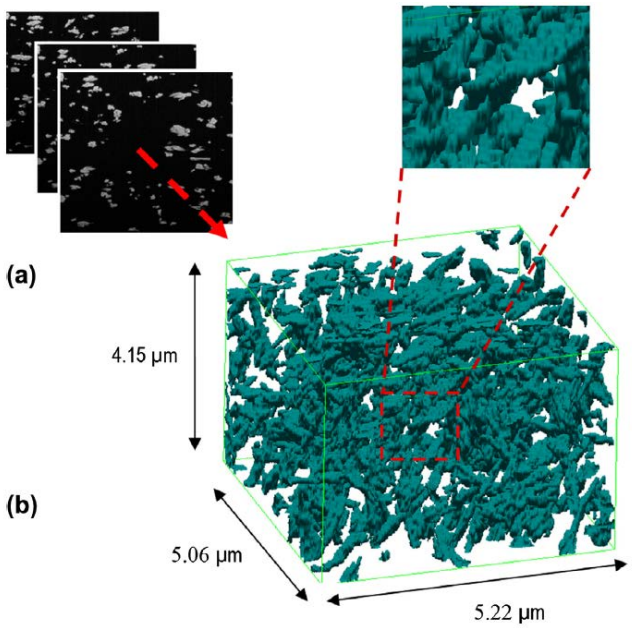

Figure 5. Schematic illustration of the 3D reconstruction process from FIB-SEM analysis. Adopted from Sheidaei et al. (2013).

2.2.1. Membrane Specifications and Characteristics

For initial development of FIB-SEM characterization procedures, one membrane was chosen for this study based on its porosity, pore diameter, thickness, and material. Table 2 shows the membrane's specifications, which were provided by the manufacturer 3M. This membrane was ideal for FIB-SEM analysis because it is relatively thick for MD membranes and has high porosity. The experimentally measured flux for this membrane, as shown in Figure 5, was also considerably different than other membranes with nearly identical specifications, making it viable for studying the influence microstructure must have on water vapor flux for MD.

Table 2. Membrane Specifications Provided by 3M Manufacturer

Manufacturer	Model	Base Material	Pore size	Thickness	Porosity
3M	0.2 μm	Polypropylene	0.59 μm*	110 μm	85%

*Bubble point pore diameter

2.2.1.1. Sample Preparation Difficulties Caused by Membrane Characteristics

While membrane distillation relies on the hydrophobicity of its membranes, this attribute leads to several challenges when mounting and preparing membrane samples for FIB-SEM analysis. The low viscosity epoxies needed to infiltrate the membrane void space are typically water-based, causing the membrane to reject infiltration. This leads to air gaps in the infiltration, which results in inadequate 2D SEM imaging. Therefore, an organic solvent is needed to accompany the epoxy to (1) even further decrease the mounting epoxy's viscosity, and (2) aid pore infiltration by reducing interactions between a water-based solvent and the hydrophobic membrane. Infiltrating and curing the membrane sample under vacuum also improves epoxy infiltration and ensures that the epoxy dries with adequate rigidity. This is because the vacuum environment causes water and the organic solvent to evaporate out of the epoxy once infiltration is complete, ensuring the membrane's void space is completely filled with epoxy only.

Conductive additives are typically added to the mounting epoxy to improve the resulting sample's electronic conductivity. These additives, however, are typically suspended in water, as well. To mix the conductive additive with the epoxy, it must first be dehydrated and resuspended in an organic solvent. Sample staining is often necessary for electron microscopy analysis because it enables distinct contrast between the solid phase and pore space (Lešer et al. 2009 and Knott et al. 2011). Most biological and organic samples use a heavy-metal salt in an aqueous solution for staining (Seligman et al. 1966 and Knott et al. 2011), but due to the hydrophobic nature of MD membranes, the heavy metal salt must be dissolved in the appropriate organic solvent.

Finally, the high porosity of MD membranes can cause issues during the mounting and sample preparation process. Figure 2 shows that the fibrous connections that make up the membrane's structure are relatively thin compared to the bulk size of the membrane. These thin, fibrous connections are susceptible to morphological changes during infiltration and/or staining preparation steps, which can compromise the accuracy of 3D reconstructions later during FIB-SEM analysis. Membrane affinity with the organic solvents and heavy metal staining solution must be analyzed to ensure that adverse morphological changes aren't observed within the membrane.

2.2.2. Sample Preparation Protocol

To avoid improper infiltration and inadequate contrast, we first developed a sample preparation protocol. To provide complete infiltration, a commercial mounting epoxy with sufficiently low mixed (resin + hardener) viscosity (Allied High Tech Products, Inc., viscosity = 300 cP) was used. Infiltration while under vacuum was unnecessary, as the mounting epoxy had a low viscosity; therefore, the sample and epoxy were cured together in a cup only after infiltration was complete to further remove any air, water, or organic solvents. This step reduces the post-infiltration sample preparation difficulty and work that infiltrating directly under vacuum entails. Figure 6 demonstrates proper infiltration results and the successful implementation of the epoxy mounting kit from Allied High Tech Products, Inc.

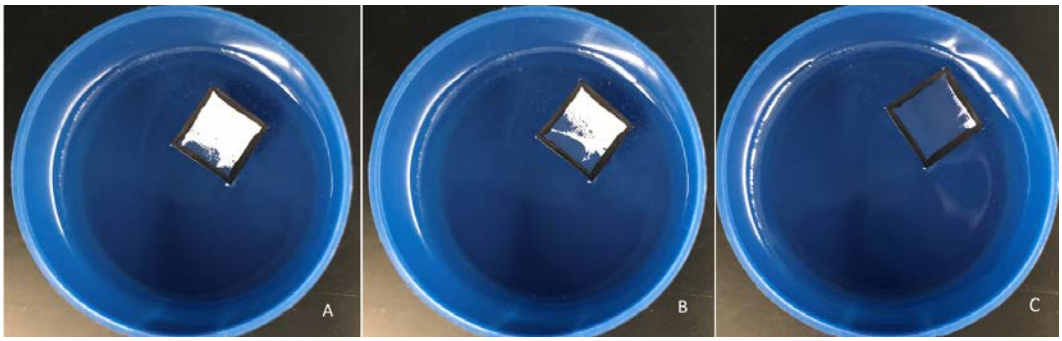

Figure 6. Time progression of infiltration testing with Allied High Tech Products, Inc.'s mounting epoxy. Time progression from (A) to (C) was 7 to 10 seconds. Notice that the membrane initially starts as a white polymer sample and finishes nearly transparent. This is caused by the membrane becoming saturated with the epoxy mixture, an attribute of full infiltration. This demonstration is done on the 3M 0.2 µm membrane.

With an epoxy mounting kit chosen, a conductive additive must be mixed with the epoxy to ensure that the epoxy has enough electronic conductivity to provide contrast during SEM imaging. For this, a conductive additive, poly(3,4-ethylenedioxythiophene)-poly(styrenesulfonate) from Sigma Aldrich was used. As purchased, this conductive additive is suspended at 1.3% in water, so it had to be dehydrated out of solution and resuspended in an appropriate organic solvent. Acetone has acceptable affinity with the conductive additive and reduces the viscosity of the epoxy once the two are mixed. The dehydration process is completed by taking 10 milliliters (mL) of the conductive additive in water in a glass vial and placing it under vacuum for 24 hours. All suspending water evaporates out, leaving only the conductive polymer particles. The conductive additive is then resuspended in 10 mL of acetone and sonicated for 60 minutes to ensure full resuspension. After 24 hours, the resuspended conductive additive ought to have a yellow supernatant fluid, as demonstrated in Figure 7. The supernatant is used as the conductive additive, and the excess polymer flakes left remaining in the suspension are not needed for mixing with the epoxy or infiltration.

Figure 7. Yellow supernatant consisting of conductive polymer additive and acetone.

During the resuspension process, the membrane sample was simultaneously stained with a heavy metal salt solution and prepared for infiltration. This step was needed, as the membrane's soft material properties led to image distortion (often referred to as "curtaining") and structural damage during FIB-SEM analysis in the absence of the heavy-metal stain. Uranyl acetate was chosen as the heavy-metal salt because of its high electronic conductivity, affinity with biological and polymer specimen, and readiness to dissolve into solution (Lešer et al. 2009, Pacheco et al 2010, Knott et al. 2011, Ruwin 2013, Kizilyaprak et al. 2015, Narayan and Subramaniam 2015, and Kremer et al. 2015). Commercially, uranyl acetate is available as a crystalline powder and therefore needs to be mixed into solution with an appropriate organic solvent. We used methanol because of its higher polarity than acetone and ethanol. Methanol also proved to have adequate affinity with the polymer membrane during the staining procedure. Once the uranyl acetate is in solution with methanol, the membrane sample can be stained via soaking in a vial with approximately 3 mL of the staining solution. The sample and vial are then sonicated for up to 1 hour to ensure complete staining of the membrane. If the membrane is not thoroughly stained, the resulting FIB-SEM analysis and 2D SEM

images can lack proper contrast and conductivity during the slice-and-view process. After staining, the sample is allowed to dry completely under room air to remove any methanol from within the membrane pores.

With the conductive epoxy mixed and the membrane sample stained, infiltration can occur. The epoxy is poured into a plastic cup, similar to that in Figure 6, prior to membrane addition. The epoxy is allowed to sit for 2 to 5 minutes to help remove any air bubbles created from mixing. The membrane is then carefully added to the epoxy to begin the infiltration process. Because the epoxy/conductive additive mixture has a low viscosity, the bulk of the infiltration occurs at atmospheric conditions. The membrane and epoxy are then gently swirled to allow the membrane to fully immerse into the epoxy. The cup is then immediately placed in the vacuum oven, where it is allowed to cure (with no added heat) for 24 hours. This step ensures the removal of the acetone, which can cause FIB-SEM analysis issues, and any remaining air bubbles in the epoxy mixture or the membrane.

After fully curing, the membrane sample is removed from the cup and prepared for cross-sectioning. First, the sample is manually cross-sectioned using a fine-toothed jeweler's saw and Dremel. Cross-sectioning allows for the infiltrated membrane to be exposed from the rest of the epoxy mount, making FIB-SEM analysis possible on the membrane. However, manual cross-sectioning leaves the surface quite rough when viewing the cross-section with the SEM. Further polishing is achieved using an ion cross-sectional polisher (JEOL IB-0910CP Cross-Section Polisher). This device uses an ion beam (like the FIB) to mill away an exposed face of a sample. The membrane sample is positioned so that the manually cross-sectioned face is polished for an additional 7 to 8 hours in the device. The result is a smooth, exposed surface that is ready for FIB-SEM analysis.

2.2.3. Sample Preparation Results

Successfully infiltrating the membrane and providing electronic conductivity is verified by manually viewing the mounted sample and via SEM analysis. As stated in the previous section, the stained membrane ought to have a yellow color once fully dried (Figure 8). During infiltration, the epoxy completely fills the void space and enhances the yellow stain (Figure 9). The sample shown in Figure 8 is now ready for both manual and ion cross-sectioning, in which the goal is to expose a section of the membrane that can be analyzed by the FIB-SEM. The initial manual cross-sectioning allows for ion polishing via the cross-sectional polisher and prevents the FIB-SEM from having to mill through excess epoxy to reach the membrane.

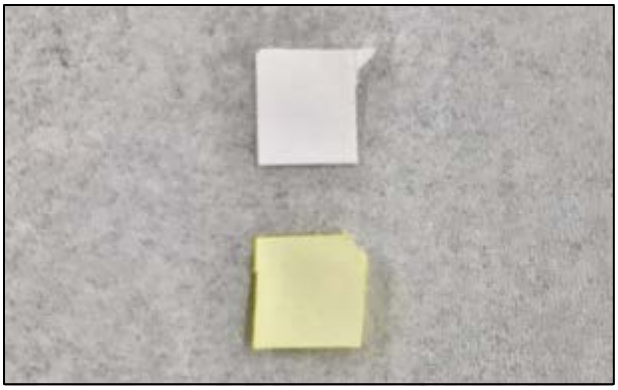

Figure 8. Stained membrane (below), compared to unstained membrane (above).

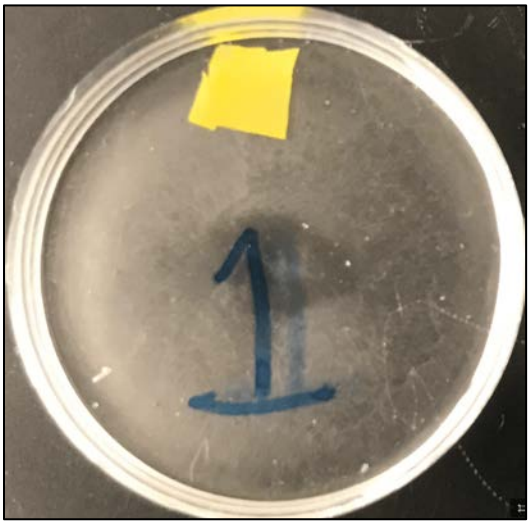

Figure 9. Fully infiltrated membrane sample. SEM analysis is used to confirm infiltration result.

Figure 10 shows an SEM view of the final cross-sectioned membrane. The membrane may look insufficiently infiltrated, but this is because of the coarse beam settings of the ion polisher, which causes slight damage to the membrane and epoxy surface. This proved not to be an issue with further FIB-SEM analysis, as the structure below the cross-sectioned membrane remained fully infiltrated.

SEM analysis confirms that the conductive epoxy efficiently provided complete infiltration and electronic conductivity at the pore-scale. FIB is briefly used to mill a section of membrane away at a region of interest (ROI) to expose the membrane cross-section below the surface. Figure 10 verifies successful contrast and infiltration. Because of the heavy-metal staining, the membrane fibers back-scatter more electrons and appear whiter, whereas the epoxy appears relatively darker in the SEM images. This ROI can now undergo the slice-and-view process. The ROI needs to remain consistent in both infiltration and contrast to obtain successful slice-and-view results.

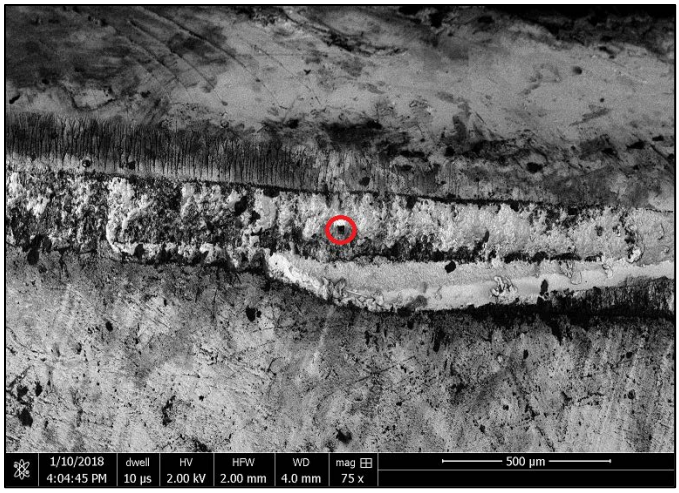

Figure 10. SEM view of 3M 0.2 µm membrane after ion polishing and cross-sectioning. The middle, rougher section represents the membrane space. Above and below are pure epoxy regions.

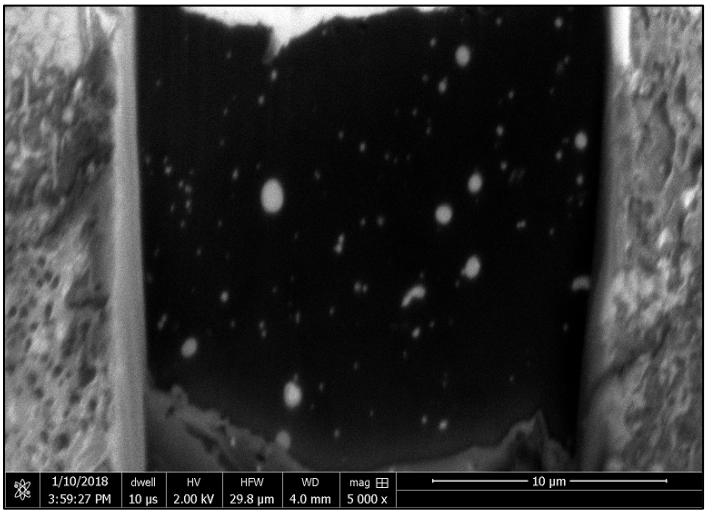

Figure 11. Exposed ROI of 3M 0.3 µm membrane via FIB. Image taken with SEM to verify infiltration and contrast. White dots represent membrane fiber cross-sections and dark areas represents epoxy-filled pore space.

2.2.4. FIB-SEM Slice-and-View Analysis

Once the mounted sample has been cross-sectioned, it is ready for FIB-SEM slice-and-view. The sample is loaded into the evacuated chamber of the FIB-SEM instrument and is first viewed with the SEM. This allows the user to identify a ROI in which milling can take place. The red circle in Figure 10 shows the ROI of the 3M 0.2 micron (µm) membrane chosen for FIB-SEM analysis. Notice the relative size of the ROI within the red circle compared to the cross-section of the membrane itself. The ROI here was chosen based on the relative fill and smoothness of the conductive epoxy.

The FIB then mills the ROI to expose the sampling face of the ROI, like the one shown in Figure 10. This serves as an investigative step to determine whether the ROI selected will yield adequate results once the slice-and-view process begins. Once the user commences the process, the sample face and ROI cannot be adjusted.

To protect the ROI from electron and ion beam damage, a platinum (Pt) pad approximately 200 to 500 nm thick is deposited over the entire region to be milled. Figure 12 shows an example of Pt deposition over a ROI. For this deposition, the ion beam was used at a current of 0.79 nA and a voltage of 30.0 kilovolts (kV). Ion beam Pt deposition provides a quicker deposition time, compared to electron beam deposition but can damage the ROI. Here, the ion beam Pt deposit will only potentially damage 100 nm below the surface of the ROI, which is reasonably shallow compared to the roughly 20 μm x 20 μm x 20 μm volume that will be sampled during slice-and-view.

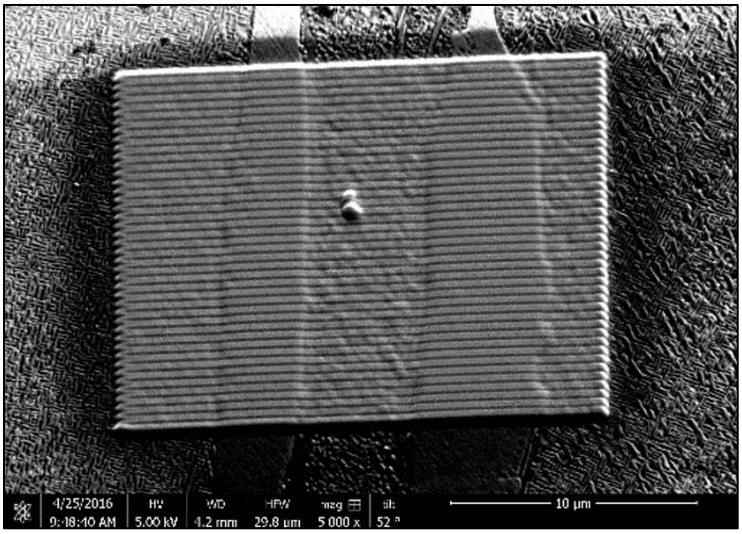

Figure 12. Pt deposition on the ROI to be imaged during slice-and-view.

After Pt deposition, trenches are milled around the ROI. This allows debris and milling waste to be collected so that the sampling face can remain unobstructed when imaging with the SEM. A rectangular cross-sectioning setting for the FIB is used at a high current and voltage (9.3 nA, 30.0 kV) for fast milling, as shown in Figure 13. Since the trenches are not a part of the sampling volume, it doesn't matter if the material is damaged at such high settings. A sloping trench in front of the sampling face is also milled at a length and depth so that the entire sampling face can be viewed at all times. The taller the sample face, the longer and deeper the front trench needs to be. Also shown in Figure 13 is a milled X, known as a fiducial point, which helps the fix the ion beam at the ROI and prevents drifting between slices. Without the fiducial point, the ion beam would move with each slice, causing the SEM to also move out of view of the sampling face. The slice-and-view program tells the ion beam to find this fiducial point and

to keep it at the exact coordinates as when the process began. After milling trenches, a cleaning rectangular cross-section setting is used at a low current (usually a factor of 3 lower than what was used to mill trenches) to clear any debris that may have collected on the face. A before and after comparison is shown in Figure 14. The sample and ROI is now prepped and ready for slice-and-view. For an imaged volume of roughly 22.96 μm x 15.30 μm x15.00 μm, a total of 750 SEM images were collected over 13 hours. The first 35 images involved the ion beam slowly moving towards the sampling face and ROI and were not used for further analysis.

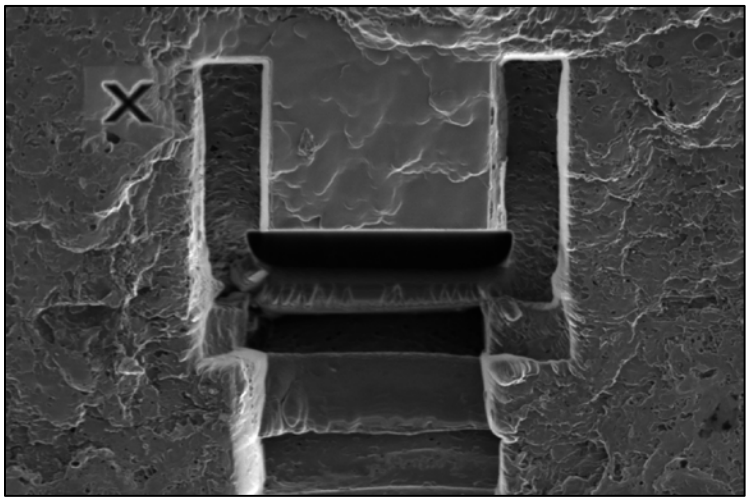

Figure 13. Milled trenches used to collect debris and milled waste during slice-and-view.

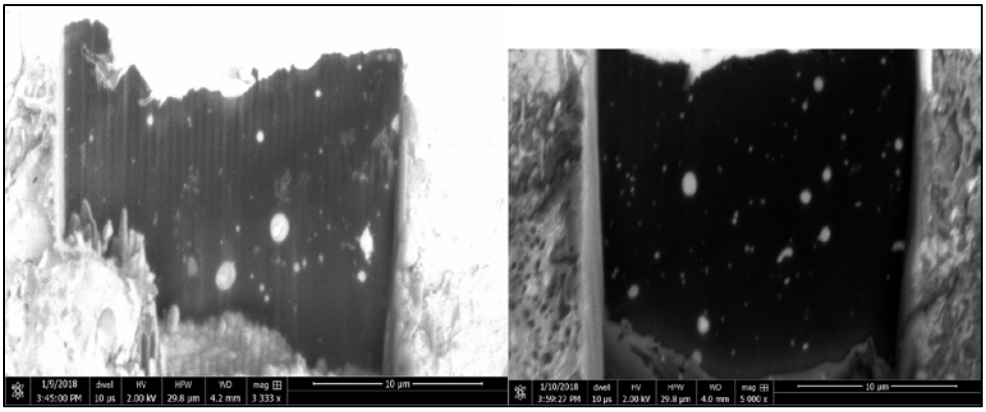

Figure 14. Left SEM image shows before the ROI and sampling face is cleaned. Right is SEM image post-cleaning.

2.2.5. Image Processing

Before the 715 usable SEM images collected can be reconstructed into a digital 3D volume, an extensive amount of image processing must occur:

- During the FIB-SEM slice-and-view data collection, the electron beam occasionally drifts and corrects itself using the fiducial. These slight oscillations are preserved when serially stacking the images as a total set. These oscillations distort the reconstruction and are non-physical within the sampled volume. The oscillations must therefore be removed for an accurate 3D reconstruction.
- Minimizing slice-and-view collection times requires stronger electron beam current and voltage values. However, these compromise the resulting SEM image resolution. For the 3D reconstruction, images must therefore be sharpened to maximize the image resolution for nm-scaled features such as membrane fibers.
- Most 3D reconstruction software needs the SEM images to be binary input (meaning black and white pixels only). This is so the software can properly differentiate between solid membrane fiber and pore space. Any unresolved, gray pixels will hinder the resulting 3D reconstruction.

Most of the SEM image processing was done using a modified MATLAB graphic user interface (GUI) provided by Ryan Collette, a Colorado School of Mines Nuclear Engineering graduate student (Collette et al. 2016). The GUI enables batch processing the SEM images with cropping, sharpening, filtering, and segmenting functions, plus the ability to transform all images into binary format. Figure 15 shows an example of the interface. Figure 16 compares a raw, unprocessed FIB-SEM image with a final processed SEM image. Once batch processing is complete, the 715 new binary images are exported and ready for further processing and 3D reconstruction.

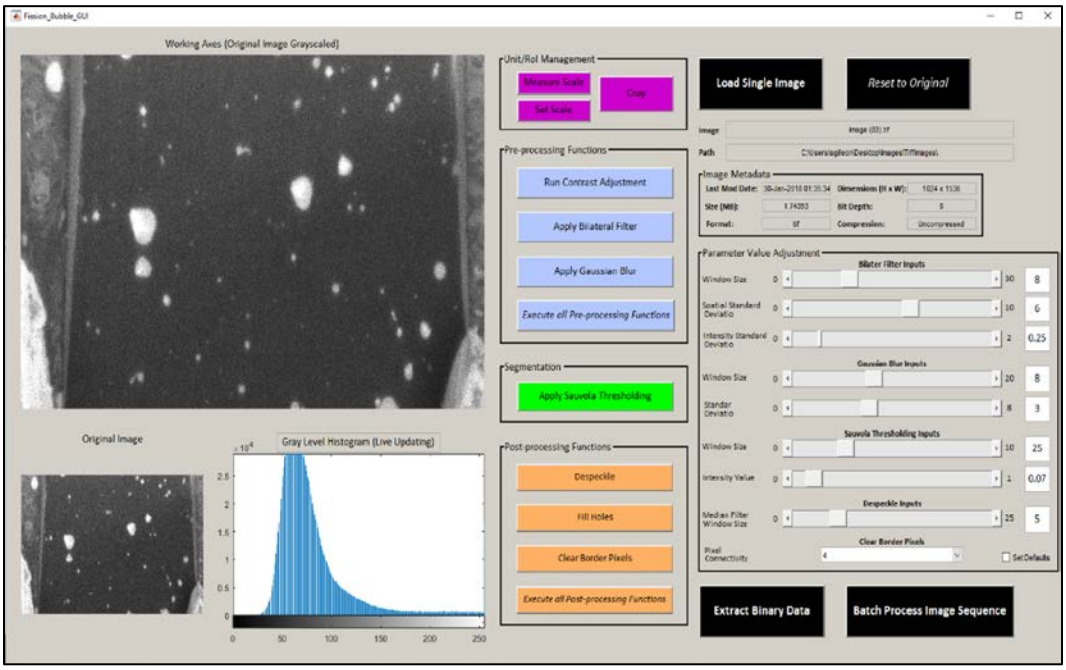

Figure 15. MATLAB image processing GUI.

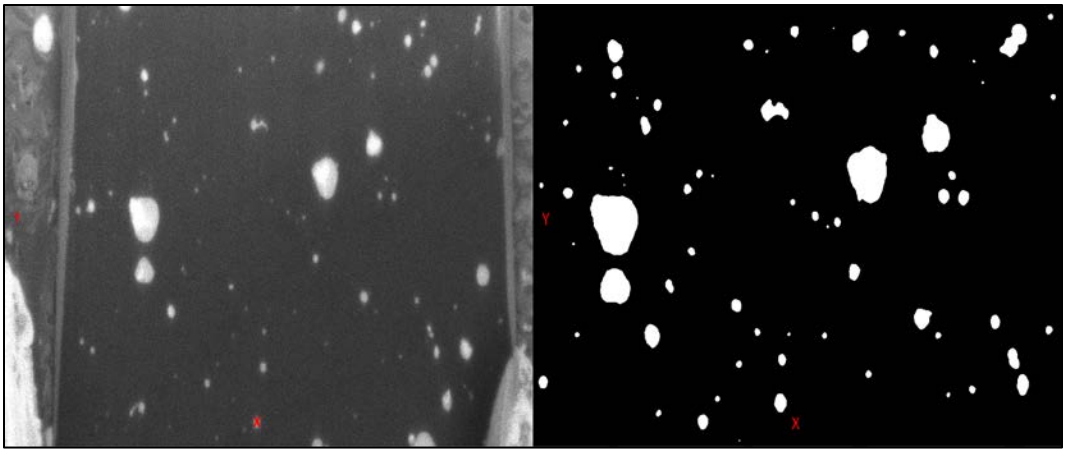

Figure 16. Before and after of SEM image once all processing steps are completed. Left image has dimensions 22.96 µm x 15.30 µm (x, y). Right image has dimensions 16.46 µm x 12.72 µm (x, y).

2.2.6. Oscillation Removal on Post-Processed Images

As mentioned in Section 2.2.4, image oscillations remaining after fiducial correction will distort the 3D reconstruction. To remove the remaining oscillations, we developed a MATLAB optimization script and used the script with an application plugin for ImageJ, a public-domain, Java-based image processing program. The MATLAB optimization and oscillation removal code uses MATLAB's Genetic Algorithm to minimize the sum of squared residuals (SSR), which evaluates the difference between any two adjacent images i and i+1 as shown in Equation 1 below:

$$SSR = \sum_{j=1}^{n_j} \sum_{k=1}^{n_k} \left(I_{i,j,k} - I_{i+1,j,k}\right)^2$$

where $I_{i,j,k}$ represents the intensity (0 = dark, 1 = light) for the pixel at the location (j, k) summed over n_j and n_k, the number of pixels in the x and y directions, respectively. For each pixel, the difference between the pixel intensity values in the two images is calculated, and the genetic algorithm solver attempts to minimize the SSR of the pixel-matrix differences for each image pair in the stack. The independent optimization variables are n_x and n_y, integer pixel movements for image $I_{i+1,j,k}$ in the x and y directions. To illustrate, consider Figure 17. The current image is on the left side, with the red box indicating the sampling window. In the next image i+1 (right side), the red sampling window is placed in the same coordinates as in I_i, but the features within the window have moved by some pixels in both the x and y directions due to the oscillation. The optimization algorithm moves the image by n_x and n_y pixels to minimize the SSR. Because the features change position and size, the minimization is unable to reach absolute zero. At the end of the algorithm, the total pixel movement values are saved and

applied to I_{i+1}, which becomes the next I_i. The process repeats for each image pair until all the images have been independently shifted and aligned. This removed most of the large oscillations present in the dataset, but small oscillations remained. To remove finer oscillations, we used ImageJ plugins called *Template Matching* and *Align Slices in a Stack*. These applications were successful in removing small oscillations, readying the dataset for 3D reconstruction.

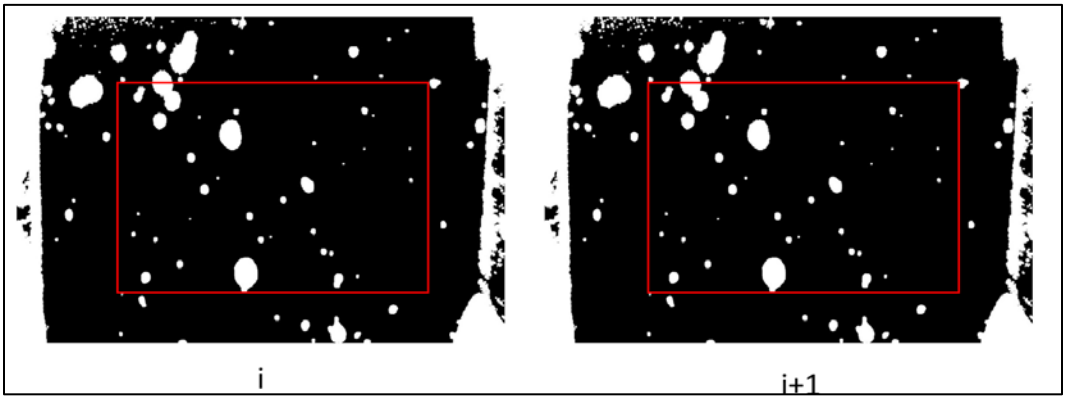

Figure 17. Current Image and Next Image with red sampling windows. The features within the windows are used to determine the SSR.

2.2.7. 3D Reconstruction and Analysis

All of the 715 binary, processed images were serially stacked and reconstructed using *Dragonfly Pro* software provided by Object Research Systems, Inc., as demonstrated in Figure 18. The only user inputs required by the software are the pixel dimensions in the *x*, *y*, and *z* directions. Based on the sampling volume dimensions and image resolution, the size of each pixel is 15 nm x 15 nm x 20 nm (*x*, *y*, *z*). The raw reconstruction is then 16.5 μm x 12.7 μm x 14.3 μm (*x*, *y*, *z*) with a total volume of approximately 2,996 μm^3.

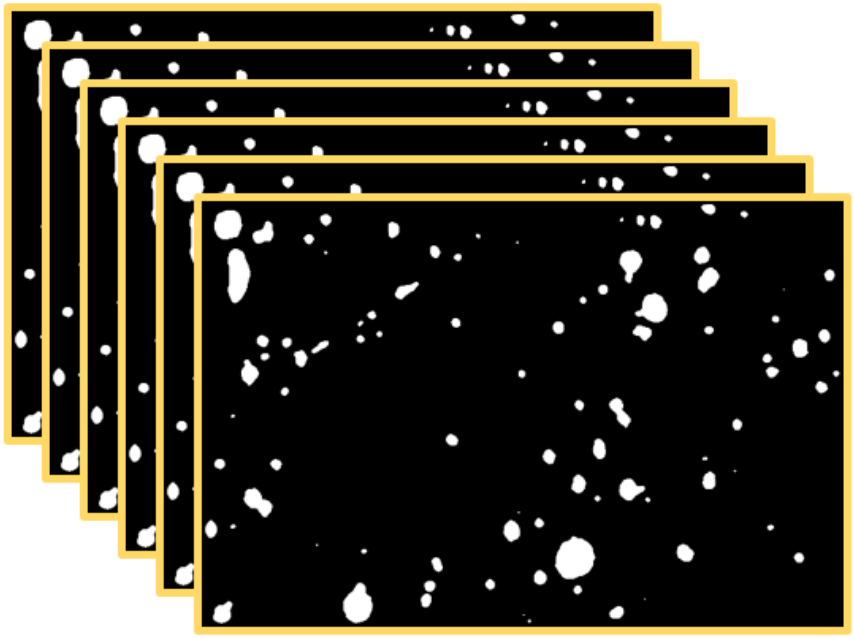

Figure 18. Stack of 2D SEM images are used to render 3D reconstructions.

2.3. Pore-Scale Transport Modeling

Concurrent to the microstructural characterization in Section 2.2, we developed a pore-scale transport modeling tool to relate the observed microstructural parameters to variations in MD performance. The modeling tool is publicly available at Dr. DeCaluwe's github profile (DeCaluwe and Gilleon 2019). The model implements time-resolved conservation equations for mass, species/elements, and energy within the membrane, and integrates these equations over a long time period to estimate steady-state behavior. This section briefly describes the model equations.

2.3.1. Continuity Equations: Species Density

Conservation of mass and elements are applied to calculate the time derivative of the gas-phase species density ρ_k (kg of k/m^3) within the pores as shown in

Equation 2:

$$\frac{\partial \rho_k}{\partial t} = -\frac{\nabla J_k}{\varepsilon_g},$$

Where:

t is time (s)

J_k is the mass flux for species k

ε_g is the volume fraction of the gas phase (i.e. the membrane porosity).

The problem is solved using a finite-volume approach, with the species properties calculated at the volume centers and the fluxes J_k calculated at the volume interfaces. At the membrane-flow channel boundaries, the flux is set equal to an evaporation/condensation interfacial reaction rate $\dot{s}_k$ as shown in Equation 3:

$$J_k|_{y=0,H} = W_k \dot{s}_k$$

Where:

W_k is the molecular weight (kg/kmol) of species *k*.

The $\dot{s}_k$ terms (which have units of (kmol/m^2/s) at each interface are solved using Cantera, an open-source library of software routines for solving problems involving thermodynamics, chemical kinetics, and transport rates. The thermodynamics and kinetic rate constants are set such that the pore volumes near each flow channel interface (feed and permeate) remain very near the saturation condition. The calculation of J_k values at interfaces within the membrane is described in Sections 2.3.3.1 and 2.3.3.2. For each volume, we note here that the total mass density can be calculated as the sum of the species densities: $\rho = \Sigma\rho_k$.

2.3.2. Energy Equation: Temperature

Conservation of energy is applied to calculate the time derivative of the local temperature *T* as shown in Equation 4:

$$\frac{\partial T}{\partial t} = -\frac{1}{\rho C_v}\nabla(\dot{q}''_{cond} + \dot{q}''_{conv} + \dot{q}''_{chem})$$

Where:

C_v is the (volume-averaged) specific heat, and

$\dot{q}''$ terms are the heat fluxes (W/m^2) due to conduction (cond), species convection (conv), and chemical reactions (chem) (i.e., evaporation and condensation at the membrane interfaces).

The calculation of the $\dot{q}''$ terms is described in Section 2.3.3.3.

2.3.3. Species Mass Transport

The species mass fluxes J_k are calculated using one of two models, in this study:

- Fickian-based molecular diffusion, in parallel with convection; and
- The Dusty Gas Model (DGM), which considers molecular diffusion and Knudsen diffusion in series, both in parallel with convection.

Because detailed information about membrane microstructures is not readily available, microstructural effects are typically incorporated empirically by fitting against experimental data. Rather than directly incorporate membrane

microstructural effects, the transmembrane flux of water vapor J_{H2O} is typically modeled on the module level, as opposed to the pore-scale level as shown in

Equation 5:

$$J_{H2O} = C_m\left(P_{H2O,feed} - P_{H2O,dist}\right)$$

Where:

$P_{H2O,feed}$ is the water saturation pressures on the feed,

$P_{H2O,dist}$ is the water saturation pressures on the distillate sides of the membrane, and C_m is the membrane permeability coefficient.

C_m is a function of the membrane thickness and microstructure and is typically treated as a fitting parameter, which prevents using any such models for predictive simulations in the membrane design process. A more sophisticated approach replaces this equation with the DGM, which considers molecular diffusion (dominated by molecule-molecule collisions) and Knudsen diffusion (dominated by molecule-wall collisions) in series, both in parallel with Darcy flow (Andrjesdóttir et al. 2013, Hitsov et al. 2015, and Shirazi et al. 2016). This standard approach of adding diffusion resistances, however, has recently come under question (Field et al. 2013) In addition, the DGM is ill-equipped to handle several phenomena relevant to MD, such as non-isothermal effects and microstructural heterogeneity (Gao et al. 2011 and Field et al. 2013).[9,30]

To explore the importance of transport mechanism in the simulation of DCMD, we implemented both Fickian diffusion and DGM models in this study.

2.3.3.1. Fickian diffusion:

The Fickian diffusion model only accounts for molecular diffusion and convection (i.e., bulk flow). Fickian diffusion models scale all transport properties (mixture-average diffusion coefficients D_k) according to the membrane microstructure as shown in Equation 6:

$$D_k^{eff} = \frac{\varepsilon_g}{\tau_g} D_k$$

Where:

τ_g is the gas-phase tortuosity factor

The Fickian diffusion model is less computationally expensive than the DGM but does not discriminate between other microstructural parameters (such as polymer fiber diameter or average pore radius), which also brings it into question for modeling MD flux transport. Moreover, the Fickian model explicitly neglects Knudsen diffusion. Depending on the Knudsen number for the selected membrane, this can be a significant error.

Fick's law calculates the diffusive flux with respect to the average velocity of the transport fluid as shown in Equation 7:

$$V_k^{Diff} = -\frac{D_k^{eff}}{X_k}\mathrm{d}_k - \frac{D_k^T}{\rho Y_k}\nabla T$$

Where:

D_k^T is the thermal diffusion coefficient

Y_k is the species mass fraction

The operator d_k is shown in Equation 8:

$$\mathrm{d}_k = \nabla X_k + (X_k - Y_k)\frac{\nabla p}{p}$$

Where: p is the gas-phase pressure.

The convective (bulk-phase) velocity V_{conv} is shown in Equation 9:

$$V_{conv} = -\frac{K_g}{\mu}\nabla p$$

Where:

K_g is the gas-phase permeability of the membrane

μ is the gas-phase viscosity.

Finally, the species mass flux $\mathrm{J_k}$ is the sum of the diffusive and convective velocities, multiplied by the species mass concentration as shown in Equation 10:

$$J_k = \rho Y_k\left(V_{diff} + V_{conv}\right)$$

2.3.3.2. The Dusty Gas Model

The DGM is an implicit relationship between the species molar fluxes, molar concentrations, and mole fraction gradients. This expression can be inverted to calculate the species mass fluxes as shown in Equation 11:

$$J_k = -W_k\left[\sum_{l=1}^{N_{gas}} D_{kl}^{DGM}\nabla[X_l] + \left(\sum_{l=1}^{N_{gas}} D_{kl}^{DGM}\frac{[X_l]}{D_{l,Kn}^{eff}}\right)\frac{K_g}{\mu}\nabla p\right].$$

In this expression, the DGM binary diffusion coefficients D_{kl}^{DGM} can be calculated as the inverse of the matrix H, the elements of which are found as shown in Equation 12:

$$h_{kl} = \left[\frac{1}{D_{k,Kn}^{eff}} + \sum_{j\neq k}\frac{X_j}{D_{kj}^{eff}}\right]\delta_{kl} + (\delta_{kl} - 1)\frac{X_k}{D_{kl}^{eff}}$$

Where:

δ_{kl} is the Kronecker delta function

The effective Knudsen diffusion coefficients are calculated as as shown in Equation 13:

$$D_{k,Kn}^{eff} = \frac{4}{3}\frac{\varphi_g}{\tau_g} r_p \sqrt{\frac{8RT}{\pi W_k}}$$

With R the gas constant and r_p the average pore radius.

2.3.3.3. Heat Transfer Terms

The heat transfer terms $\dot{q}''_{cond}$, $\dot{q}''_{conv}$, and $\dot{q}''_{chem}$ are calculated using mostly standard, volume-weighted approaches, as reported in this section.

Conductive heat fluxes are calculated using a volume-weighted average thermal conductivity κ_{avg} as shown in Equation 14:

$$\dot{q}''_{cond} = -\kappa_{avg} \nabla T.$$

The so-called "convective fluxes" $\dot{q}''_{conv}$ are due to the mass fluxes of species within the membrane pores as shown in Equation 151:

$$\dot{q}''_{cond} = -\nabla \left(\sum_{k=1}^{N_{gas}} h_k J_k \right).$$

Finally, the "chemical" heat flux is due to the heat of evaporation/condensation h_{fg} at the membrane boundaries as shown in Equation 162:

$$\dot{q}''_{chem} = \begin{cases} -0.5\, J_{\mathrm{H2O}} h_{fg} & y = 0 \\ 0.5\, J_{\mathrm{H2O}} h_{fg} & y = H \\ 0 & otherwise \end{cases},$$

Where the factor of 0.5 reflects the assumption that the heat of reaction is divided evenly between the membrane and the water in the flow channel.

2.3.3.4. Microstructure and methodology

The tortuosity factor, τ_g, clearly plays a significant role in determining performance of MD membranes, as it arises in all three transport mechanisms. However, this membrane parameter is not well understood and is not easily measured, unlike porosity and pore radius. An empirical correlation first proposed by Mackie and Meares and often cited in literature (Alves and Coelhoso 2004, Srisurichan et al. 2006, and Rao et al. 2014) is used to calculate tortuosity factor, as shown in Equation 17:

$$\tau_{corr} = \frac{(1-\varepsilon_g)^2}{\varepsilon_g}.$$

For both the Fickian and DGM mass flux models, the simulation tool was used to predict the trans-membrane water flux for a range of tortuosity factors, including τ_{corr} above, over the range of feed and permeate temperatures probed in the bench-scale experiments. Comparing modeled with experimentally measured water fluxes provides insight into the transport mechanisms controlling transmembrane fluxes in MD membranes.

2.4. Bench-Scale CFD

2.4.1. Governing Equations and Numerical Method

We considered a 2D plate-and-frame system with a feed and distillate channel of length L and height H, as in Figure 19. NaCl solution enters the feed inlet with temperature T_{in}^{f}, concentration c_{in}^{f}, and mean velocity U_{in}. Pure water enters the distillate inlet with temperature T_{in}^{d} and mean velocity U_{in}. We consider both co- and counter-current arrangements. Though Figure 5 shows the membrane as a shaded region, we model membrane transport using effective interface conditions that couple the feed ($0<y<H$) and distillate ($-H<y<0$) channels.

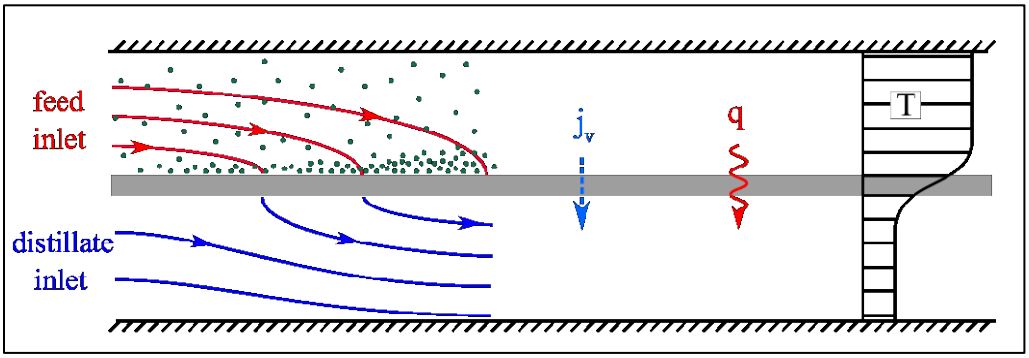

Figure 19. CFD geometry.

We assume the vapor mass flux, j_v, is linearly proportional to the transmembrane vapor pressure difference (Lawson and Lloyd 1997) as shown in Equation 18.

$$j_v = A(p_m^f - p_m^d)$$

Where:

A is the membrane mass transfer coefficient

p_m^f is the water vapor pressures on the feed sides of the membrane

p_m^d is the water vapor pressures on the distillate sides of the membrane, respectively.

As is common in the literature, we assume that *A* is a constant for a given membrane (Schofield 1987 and Yu et al. 2011). We determine A by fitting to experiments described in Section 2.3.3. We evaluate the vapor pressures as the product of the saturation pressure P^{sat} and activity a_w as shown in Equation 19:

$$P_m = a_w P^{sat}, \qquad P^{sat} = \exp\left[23.238 - \frac{3841}{T_m - 45}\right]$$

Where:

T_m is the local temperature on the membrane surface.

The activity is determined from Equation 20, (as described in Hitsov [2015]):

$a_w = 1 - 0.03112b^2 - 0.001482b$

Where:

b is the NaCl molality (mol/kg).

Assuming complete rejection, $b = 0$ in the distillate.

As in most previous literature, we model the transmembrane heat conduction as Equation 213:

$$q_c = \frac{k_m}{\delta}\left[T_m^f - T_m^d\right]$$

Where:

k_m is the membrane thermal conductivity

δ is the membrane thickness

T_m^f is the membrane local feed temperature

T_m^d is the membrane distillate temperature

We treat k_m/δ as a heat transfer coefficient that is determined experimentally in Section 2.3.3. Conservation of energy at the feed surface is consequently calculated as shown in Equation 22:

$$-k\frac{\partial T_m^f}{\partial y} = j_v\lambda + \frac{k_m}{\delta}\left[T_m^f - T_m^d\right]$$

Where:

k is the thermal conductivity of the liquid

A similar condition is applied at the distillate surface, though not shown in this discussion for brevity.

Fluid flow in the feed and distillate channels is governed by the incompressible continuity and Navier-Stokes equations as shown in Equation 23:

$$\nabla \cdot \mathbf{u} = 0, \quad \rho\left[\frac{\partial \mathbf{u}}{\partial t} + (\mathbf{u} \cdot \nabla)\mathbf{u}\right] = -\nabla p + \nabla \cdot (\mu \nabla \mathbf{u})$$

Where

u = [*u v*] is the fluid velocity vector

p is the fluid pressure

ρ is the fluid density

μ is the fluid viscosity.

In the feed and distillate channels, we set the density to those measured at the inlets. Heat transport is governed by the energy equation, Equation 24:

$$\rho c_p\left[\frac{\partial T}{\partial t} + (\mathbf{u} \cdot \nabla)T\right] = \nabla \cdot (k \nabla T)$$

Where:

c_p is the fluid heat capacity

k is the thermal conductivity

NaCl transport is modeled using the advection-diffusion equation, Equation 25:

$$\frac{\partial c}{\partial t} + (\mathbf{u} \cdot \nabla)c = \nabla \cdot (D \nabla c)$$

Where:

D is the mass diffusivity.

Though we approximate the flows as incompressible, we include variations of all other thermo-physical properties with temperature and solute concentration. We derived correlations for μ, c_p, and λ using the commercial database OLI Stream Analyzer. We obtained correlations for *k* and *D* from literature (Harned and Hildreth 1951 and Ramirez and Castro 1994).

At the plates, we apply the no-slip, no-penetration, and no-flux conditions as shown in Equation 26:

$$u = v = \frac{\partial c}{\partial y} = \frac{\partial T}{\partial y} = 0, \quad \text{at } y = \pm H.$$

On the membrane surfaces, we apply the no-slip condition, $u = 0$. The remaining membrane conditions are determined from the transmembrane transport models. At the channel inlets, we apply the desired temperatures and concentrations, and fully developed laminar velocity profiles with desired mean flow velocities U_{in}, as shown in Equation 27:

$$u = \frac{3U_{in}}{2}(1 - \frac{y^2}{H^2}), \quad v = 0, \quad T = T_{in}, \quad c = c_{in}.$$

At the channel outlets, we apply well-known convective conditions (Sani and Gresho 1994) to the flow fields. At time $t = 0$, we set the flow fields to the inlet conditions.

The governing equations are discretized spatially using second-order finite-volume methods and discretized temporally using a second-order semi-implicit method (Ferziger and Peric 2002). The pressure is evaluated using an efficient, non-iterative, projection method (Choi and Moin 1994). Our choice of methods produces an efficient CFD code tailored to simulating unsteady heat and mass transport. While our results focus on steady-state cases, our implementation is based on ongoing work focused on unsteady mixing generated by feed spacers and a new approach to mitigating scale formation through feed temperature reversal (Hickenbottom and Cath 2014).

2.4.2. Experimental Calibration and Validation

To determine the coefficient k_m/δ and vapor permeability A, we performed a series of experiments using the 10-channel acrylic flow cell to measure the net vapor flux $\dot{V_{net}}$ for feed temperatures between 30 and 60 °C, as illustrated in Figure 20. The inlet distillate temperature was fixed at 20 °C, the feed concentration was set to 1 g/l, and the inlet velocity U_{in} set to 0.124 m/s. From these measurements, we determined k_m/δ = 576.72 W/(m^{2}K) using the thermal model developed by Schofield et al. (1987) and Vanneste et al. (2018). We then performed equivalent CFD simulations to determine the permeability A that best fit the experiments. In this manner, we set A=1.8676e-6 kg/(m^2 s Pa). Figure 20 demonstrates that our CFD shows excellent agreement with our experimental measurements, producing a relative error on the order of 1 percent.

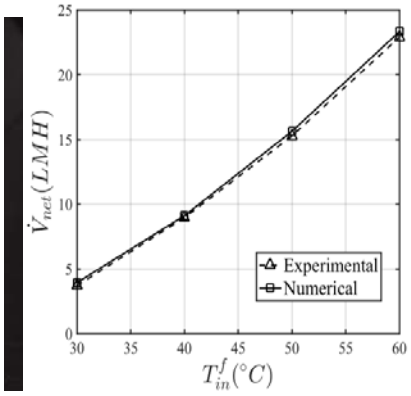

Figure 20. Experimental calibration and validation.

3. Results and Discussion

3.1. Membrane Characterization

To characterize the 17 DCMD membranes, we set the feed and distillate temperatures to 60° C and 20° C, respectively, with equal inlet flow rates of 1.6 liters per minute (L/min). This corresponds to an average channel velocity of 13 centimeters per second (cm/s). Because of the similar channel geometry, flow velocity, and spacer, the pressure drop along the distillate and feed channels should be similar. As a result, we used co-current operation to assure a similar pressure differential along the membrane. To monitor membrane integrity and calculate rejection, a small amount of NaCl was added to the feed solution. Three L of 1 g/L NaCl was used for the feed, and 3 L of deionized water for the distillate.

3.1.1. Membrane Flux

Figure 21 demonstrates that the large spread in membrane properties yields a large spread in membrane water flux. Despite the large spread, the flux of individual membranes was reproducible. All the membranes, except the 3M 0.45 micron membrane, had a standard deviation of less than 10 percent.

The CLARCOR QM902 membrane exhibited the highest flux of 49.4 liters per meter squared per hour (LMH) and the Celgard 2400 membrane exhibited the lowest flux of 3.9 LMH. There is only a very small decrease with the second best membrane, namely the 3M 0.2 micron with a flux of 49.3 LMH. Overall, all 3M membranes exhibited very high fluxes mainly due to the absence of a support layer. The 3M 0.45 micron and 3M ECTFE membrane had flux rates of 46.1 and 44.7 LMH respectively. The ECTFE membrane still managed to achieve a very high flux despite its low porosity of (67 percent), as it is thin (46 microns).

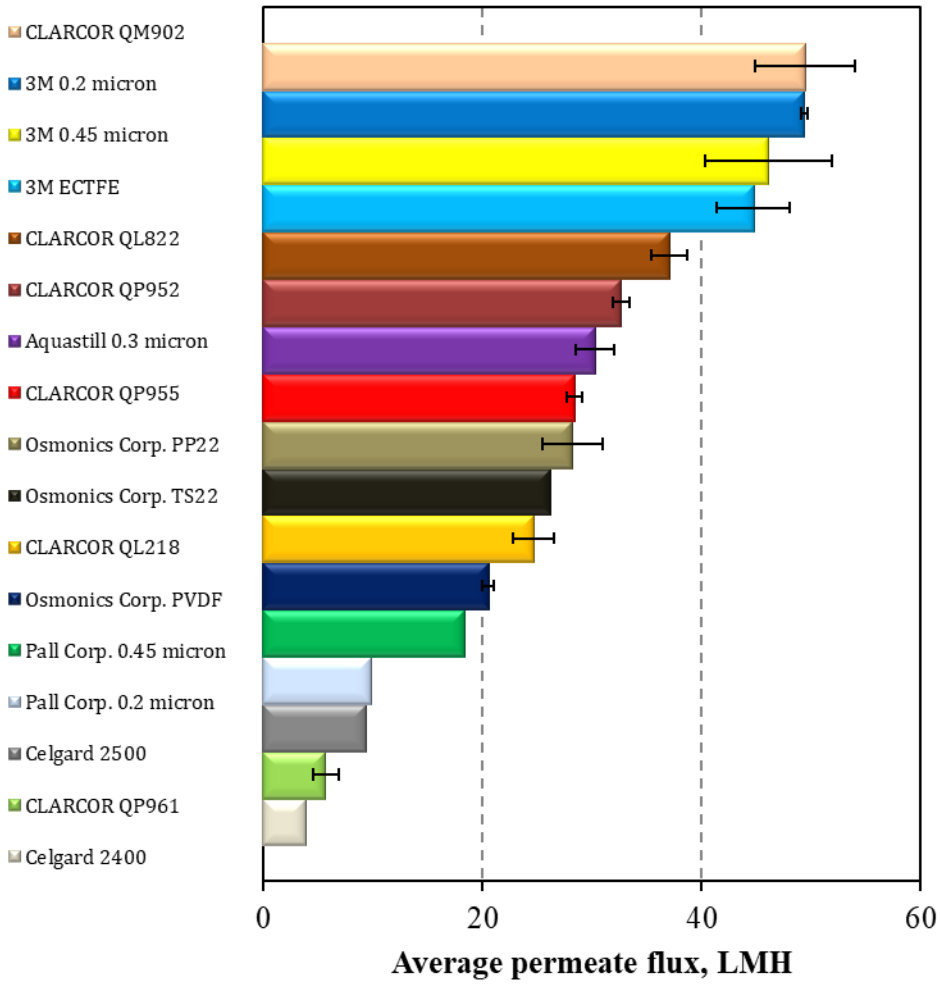

Figure 21. Comparison of water flux for the different membranes. Standard deviation is based on three different membrane samples.

As expected, the CLARCOR QM902 had a higher flux than the other CLARCOR membranes, which all include a support layer. Other results included:

- QL822, the membrane with the same active layer, but a polypropylene backing, had a flux of only 37.0 LMH compared to 49.3 LMH for just the active layer.
- QP952, the membrane with the same active layer, but with a polyester backing, had a slightly lower flux of 32.7 LMH. However, the QP952 membrane is also significantly thicker (300 microns versus 203 microns for QL822).
- QL218, the membrane with the same thickness (305 microns) and active layer pore size (0.45 micron), but with a polypropylene backing, had a significantly lower flux of 24.7 LMH. This suggests that the

polypropylene backing has a higher mass transfer resistance compared to the polyester backing.

- QP955, the membrane with the same thickness and polyester backing, but a much lower pore size of 0.1 micron, also had a lower flux of 28.4 LMH.
- The CLARCOR QP961 membrane has the smallest pore size of 0.05 micron and also had the lowest flux of 5.7 LMH. This membrane also had an oleophobic active layer.
- Aside from the CLARCOR products, the only other membrane that is marketed for MD applications is the Aquastill membrane. This membrane is unsupported (i.e., it does not have a structural support layer); however, the flux of 30.3 LMH is even lower than the flux of the two supported CLARCOR membranes with the QM902 active layer, namely QL822 and QP952. Although the membrane had one of the highest porosities (85 percent) and one of the lowest thicknesses (76 micron), it also had one of the smallest pore sizes (0.3 micron). Nevertheless, of all the tested membranes, it still had a flux significantly above the average (>26.7 LMH).

3.1.2. Membrane Thermal Efficiency

The thermal efficiency is the ratio of the convective heat transfer to the total convective and conductive heat transfer through the membrane. Accordingly, a thermal efficiency of unity would be the ideal case for an MD membrane. As can be expected, there should be a strong correlation between the water flux and the thermal efficiency. Figure 22 confirms that a trend in thermal efficiency is observed that is similar to the trend in water flux.

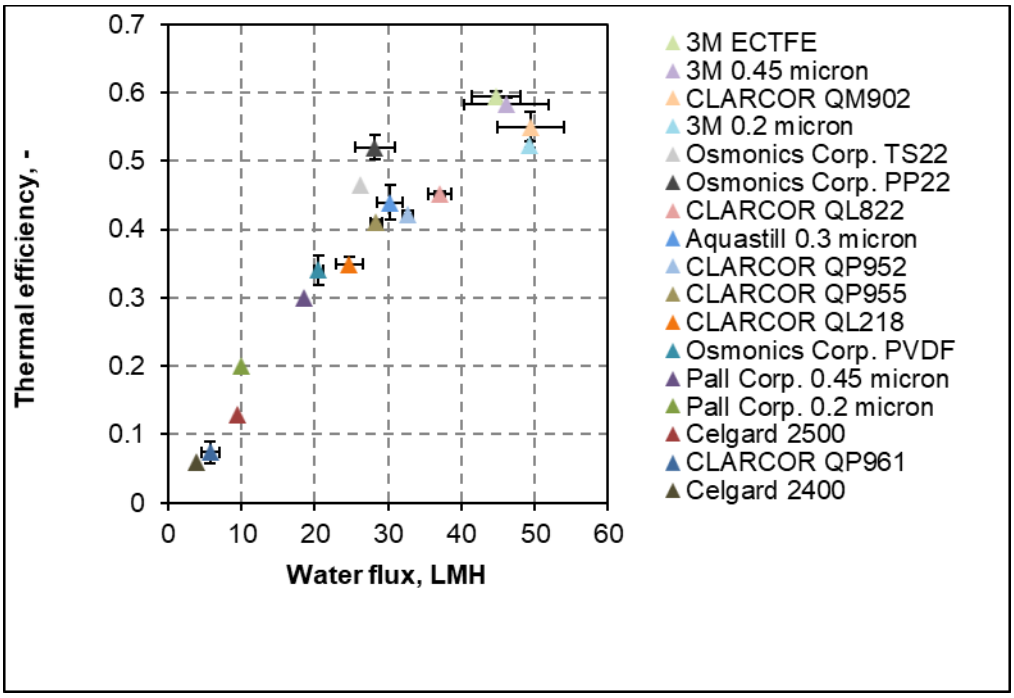

Figure 22. Thermal efficiency versus water flux.

The 3M membranes and the CLARCOR QM902 membrane that exhibited the highest fluxes also demonstrated the highest thermal efficiencies, well over 50 percent. The 3M ECTFE had the highest thermal efficiency of 59.5 percent. Conversely, the Celgard 2400 membrane had the lowest (6 percent). As a result, a Celgard 2400 membrane would require 10 times more energy for operation than a 3M ECTFE membrane.

3.1.3. Rejection and Contact Angle

The membranes were also characterized in terms of salt rejection and contact angle (see Figure 23). Most had rejections above 99.8 percent. Osmonics PVDF and Celgard 2400 had much lower salt rejections of 74 and 24 percent, respectively (not shown). Based on the surface tension of the solid polymers, the contact angle should increase in the order noted in Equation 28:

PP (32 mN/m) < ECTFE (31 mN/m) << PVDF (25 mN/m) < PTFE (31 mN/m).

Membranes with PTFE active layers indeed had higher contact angles than those with an active layer of PVDF.

3.1.4. Selection of Membranes for FIB-SEM Study

The six membranes shaded in Table 2 were selected for FIB-SEM characterization and numerical simulation. We chose non-supported membranes to focus on the effects of membrane microstructure on mass and heat transfer, rather than trying to disentangle these effects from those of the support layer. The

membranes selected cover a range of manufacturers (three from 3M and one each from Clarcor, Celgard, and Aquastil), materials (polypropylene, ECTFE, and ePTFE), and thicknesses.

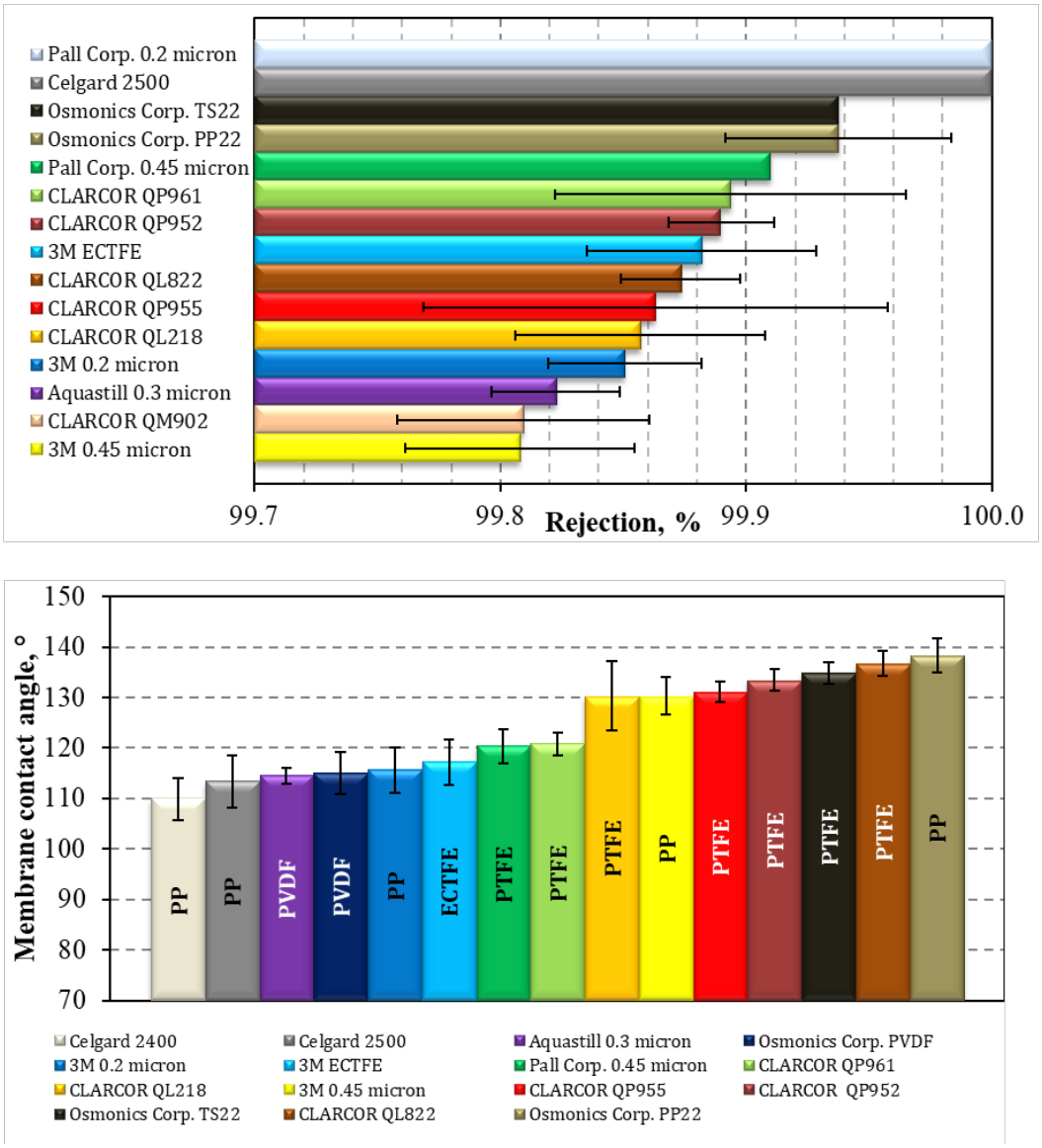

Figure 23. Salt rejection and contact angle.

3.2. Pore-scale Microstructure

The 3D iso-structure resulting from the FIB-SEM analysis described in Section 2.2 is shown below in Figure 24. As seen in the figure, the reconstruction appears to be made up of only floating solids with a spherical shape. It is hard to make out in the reconstruction whether there are membrane fibers connecting these solids. The reconstruction software calculates that the 3D volume is 95 percent porous overall. This is roughly 10 percent higher than the membrane's reported porosity

of 85 percent. We hypothesize that the 10 percent increase in pore space, relative to the reported value, is due to the inability to resolve the smaller membrane fibers using the current approach. The membrane is a soft polymer material and is perhaps unable to withstand the ion beam current needed for slice-and-view analysis. An alternate explanation is that the fiber thickness (roughly 30 nm, as seen in Figure 2) is simply thinner than the SEM resolution for this application. Therefore, physically what is present in the volume are the bundle regions where many smaller fibrous connections come together. We hypothesize that resolving the fibers would increase the solid space by 10 percent to give the sampled volume the previously reported porosity value of 85 percent.

Without fiber connections within the volume, it becomes difficult to use the 3D reconstruction for direct CFD simulations. Beyond the inaccurate microstructural parameters, with no solid connections between these bundle regions, heat transfer cannot be properly analyzed with any validity. The conductive heat transfer through the solid material—which may play a significant role in heat transfer—will not be properly accounted for in any such simulation.

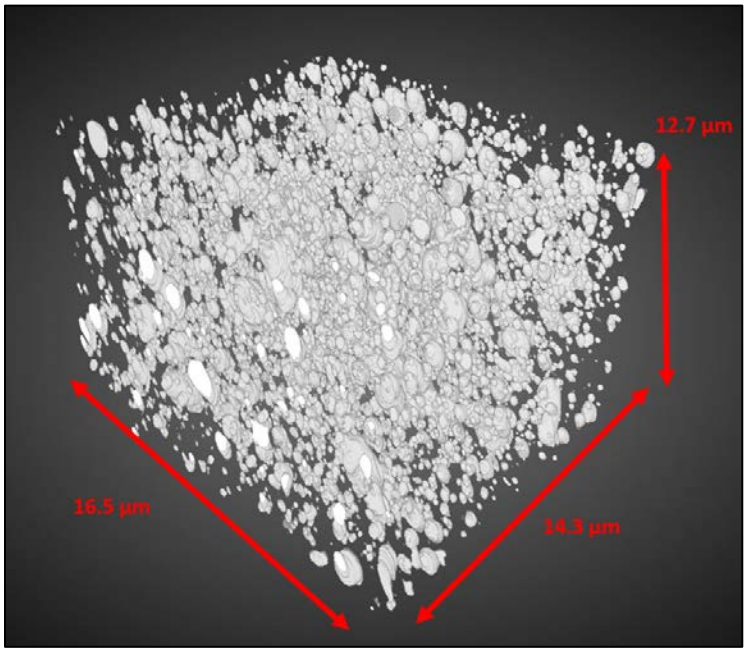

Figure 24. Raw 3D reconstruction of MD membrane. The reconstruction clearly captures regions where fibers bundle together, but appears not to accurately capture the thinner, fibrous connections between these bundles.

We attempted to post-process the raw 3D reconstruction to make pseudo-fibrous connections within the volume. This was done using a grow-and-erode technique in the ANSYS Fluent environment. The technique grows each feature within the volume using a surface wrap. The user specifies the amount to grow the features (usually until surrounding solid bodies come into contact with one another). With the features in contact, the surface wrap then erodes the solid bodies back to the

original size while retaining solid connections between each solid body. To perform this task in a reasonable amount of time, only a portion of the raw 3D volume was used.

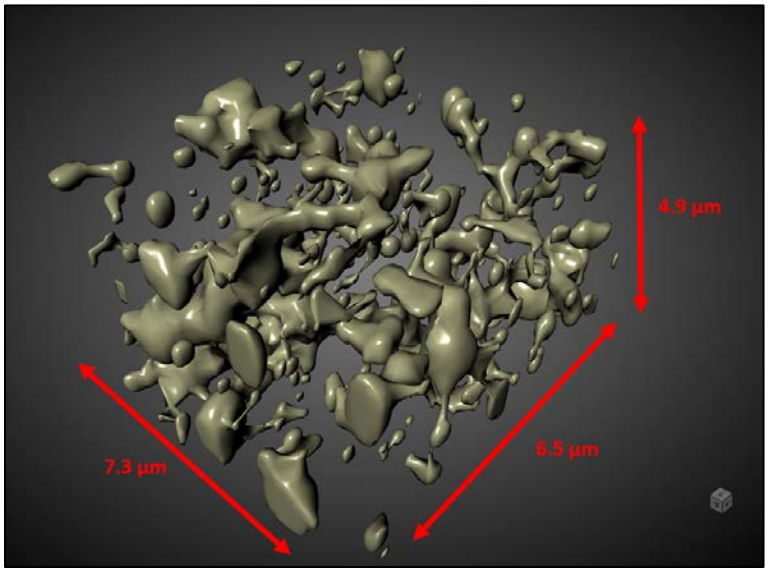

Figure 25. Partial 3D reconstruction after the grow and erode process. The resulting microstructure does not accurately represent the fibrous network shown in standard 2D SEM images.

Figure 25 shows the resulting microstructure after the grow-and-erode procedure. The new pseudo-fibrous connections do not accurately resemble the true fibrous connections. Considering this, the grow-and-erode 3D reconstruction was not used for further analysis. Although the original raw 3D reconstruction (in Figure 24) is more porous than specified from the membrane manufacturer, it can still provide useful insight into the influence of microstructure on mass transport across MD membranes.

Table 3 lists parameters extracted from the raw 3D reconstruction that are useful for 1D transport modeling and flux prediction. Pore size was measured by calculating the distance between each solid fiber and its nearest set of neighbors in 2D SEM images. The tortuosity factor was determined using a MATLAB application, TauFactor, developed by Cooper et al. (2016). TauFactor takes a stack of 2D SEM images, directly simulates transport through the structure, and outputs the tortuosity factor needed to rectify the predicted species fluxes $J_{k,theory}$ with the simulated flux $J_{k,sim}$ as shown in Equation 29:

$$J_{k,theory} = -\varepsilon_g D_k \nabla X_k = J_{k,sim} = -\frac{\varepsilon_g}{\tau_g} D_k \nabla X_k$$

Table 3. Membrane Parameters Measured from FIB-SEM 3D Reconstruction. Tortuosity Factor Provided via TauFactor

Manufacturer	Model	Pore size	Tortuosity factor	Porosity
3M	0.2 µm	0.78 µm	1.02	94.8%

Source: Cooper et al. 2016

Due to the very high porosity value in the reconstructed microstructure, the reported tortuosity factor value in Table 3, τ_g = 1.02, is likely anomalously low. Porosity was measured using volume analysis in the Dragonfly Pro software developed by Object Research Systems, Inc. A porosity profile is shown in Figure 26. While the porosity varies within the 3D reconstruction, it does not deviate by more than ±3 percent from the average porosity value of 94.8 percent (Table 3). Therefore, moving forward and for implementation into transport modeling, the average porosity value is used to represent the full microstructure.

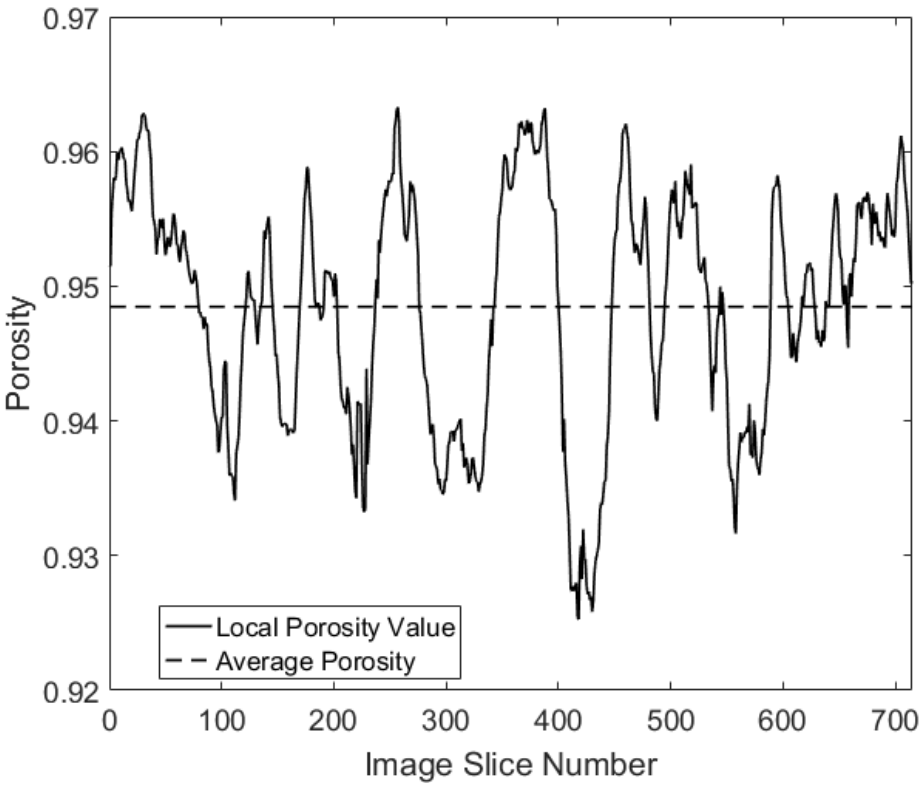

Figure 26. Porosity profile through the thickness of the 3D reconstructed membrane (in the direction of the milling).

3.3. Pore-scale Transport Simulation

For a specified temperature range (T_{feed} = 60°C, T_{perm} = 20°C), Figure 27 demonstrates the predicted flux curves for membrane parameters predicted by FIB-SEM (Table 3) and also using the manufacturer-provided parameters (Table 2). On this plot, multiple tortuosity factors are labeled on each curve. The square marker corresponds to the tortuosity factor that is directly extracted from the 3D reconstruction by the MATLAB application TauFactor. The triangle marker uses τ_{corr} from the equation above. The circle markers show the tortuosity factor value needed for each simulation to match the experimental flux given by AQWATEC for the specific temperature range (Section 3.1). The exact tortuosity factors shown on the plot can be seen in Table 4. The predicted fluxes using the FIB-SEM predicted tortuosity factor are extremely high compared to the experimentally measured flux, implying that the measured tortuosity factor is not correct due to the unresolved fibers within the reconstruction.

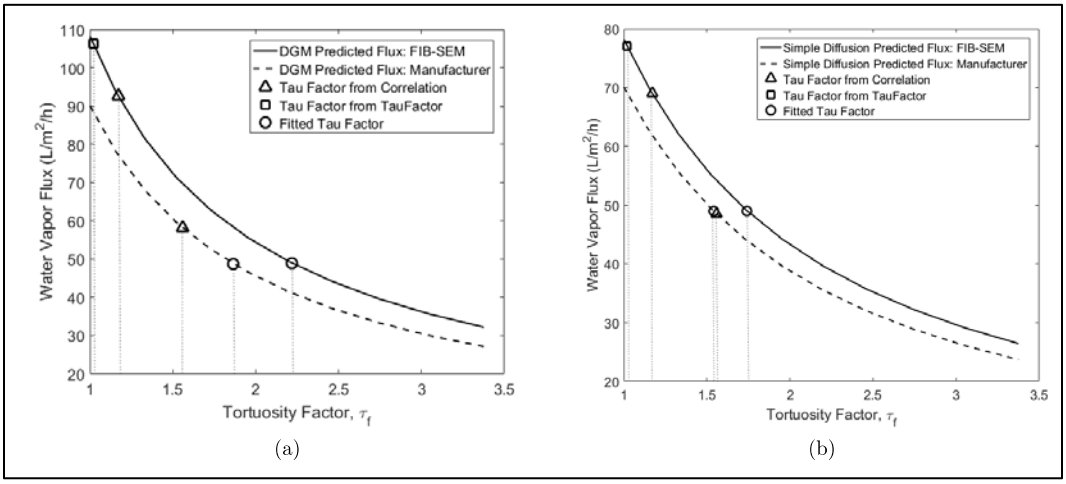

Figure 27. Predicted flux curves for (a) DGM and (b) Fickian diffusion models with varying tortuosity factor. The grey vertical lines help visualize each of the highlighted tortuosity factors. For all simulations, T_{feed} = 60°C, T_{perm} = 20°C.

Table 4. Tortuosity Factor Values for Each Set of Microstructure Parameters (FIB-SEM or Manufacturer) and Transport Model Used (DGM or Fickian).

Microstructure / Transport model	TauFactor	τ_{corr}	Fitted
FIB-SEM / DGM	1.02	1.17	2.22
Manufacturer / DGM		1.56	1.86
FIB-SEM / Fickian	1.02	1.17	1.74

Microstructure / Transport model	TauFactor	τ_{corr}	Fitted
Manufacturer / Fickian		1.56	1.54

3.3.1. Comparison between DGM and Fickian Transport Models

Table 3 and Table 4 compare the simulated and experimentally measured fluxes using the DGM and Fickian transport models, respectively. The FIB-SEM measured microstructural parameters are used for all simulations. For the 3M 0.2μm membrane, the average Knudsen number for the temperature range in this study is shown in Figure 28. The Knudsen number λ is the ratio of the mean free path to the average pore diameter and reflects the relative importance of molecular diffusion (λ >> 1) and Knudsen diffusion (λ<<1). The average Knudsen number for this membrane is approximately 0.18 and λ >0.01 for all possible average temperatures within the membrane. A Knudsen number close to 1.0, as in these simulations, typically indicates that the DGM is appropriate for simulating water vapor flux for this project.

Table 5. Comparison between Simulated Experimentally-Measured Fluxes Using the DGM TRANSPORT Model and FIB-SEM Measured Microstructural Parameters

T_{feed} (°C)	T_{perm} (°C)	J_{sim} (L/m²/h)	J_{exp} (L/m²/h)	Absolute Error (L/m²/h)	Relative Error (%)
30	20	7.2	5.9	1.3	22
40	20	18.9	15.6	3.3	21
50	20	35.1	29.3	5.8	20
60	20	58.2	49.0	9.2	19
40	30	10.8	8.9	1.8	20
50	30	26.4	22.1	4.3	19
60	30	48.5	40.9	7.6	18
70	30	77.6	66.1	11.5	17

Table 6. Comparison between Simulated Experimentally-Measured Fluxes using the Fickian Transport Model and FIB-SEM Measured Microstructural Parameters

T_{feed} (°C)	T_{perm} (°C)	J_{sim} (L/m²/h)	J_{exp} (L/m²/h)	Absolute Error (L/m²/h)	Relative Error (%)
30	20	6.6	5.9	0.7	12
40	20	17.4	15.6	1.8	12
50	20	32.7	29.3	3.4	12
60	20	54.7	49.0	5.7	12
40	30	10.0	8.9	1.1	12
50	30	24.7	22.1	2.6	12
60	30	45.7	40.9	4.8	12
70	30	73.7	66.1	7.6	12

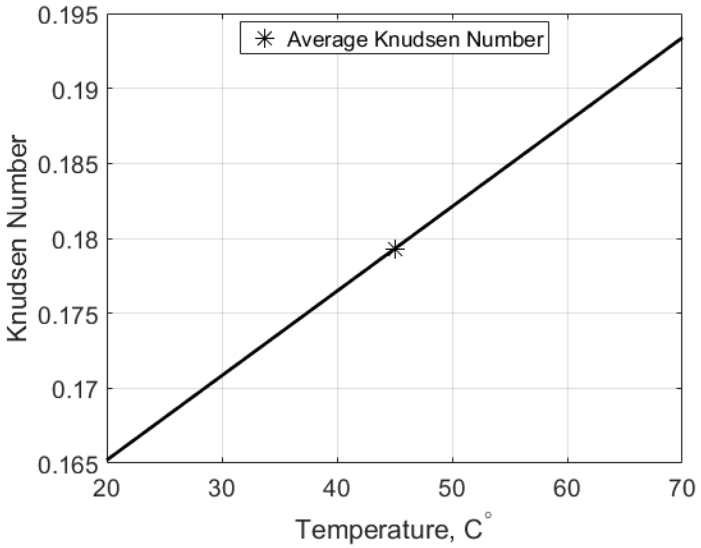

Figure 28. Knudsen number over the relevant temperature range.

Even though Knudsen number analysis suggests that the DGM is required, Table 5 and Table 6 demonstrate that the Fickian model has a smaller and more consistent relative error for each temperature range. Moreover, the species and temperature profiles from the DGM simulations, as Figure 29 and Figure 30 demonstrate, nearly linear gradients for temperature and composition. Linear species gradients further support the hypothesis that a simpler Fickian model can be used without any loss in accuracy or predictive capability. The Knudsen number dictates that all three transport mechanisms are present in the system, but

a Fickian-based diffusion model better describes and predicts the flux compared to the DGM. These results therefore imply that the Knudsen number is not an appropriate indicator of relevant transport mechanisms in MD membranes. It is quite likely, due to the thin and fibrous nature of the MD membranes, that the average pore diameter is not a representative length scale for pore-scale transport. Future work should extend this work to determine a suitable characteristic length scale for these microstructures.

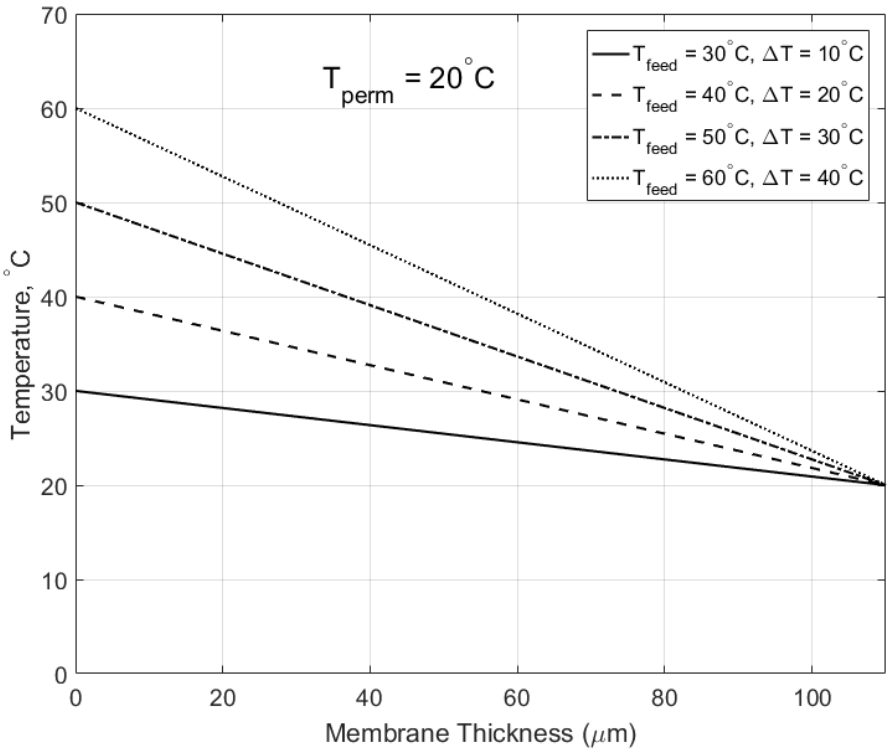

Figure 29. Temperature profiles for T_{perm} = 20° C.

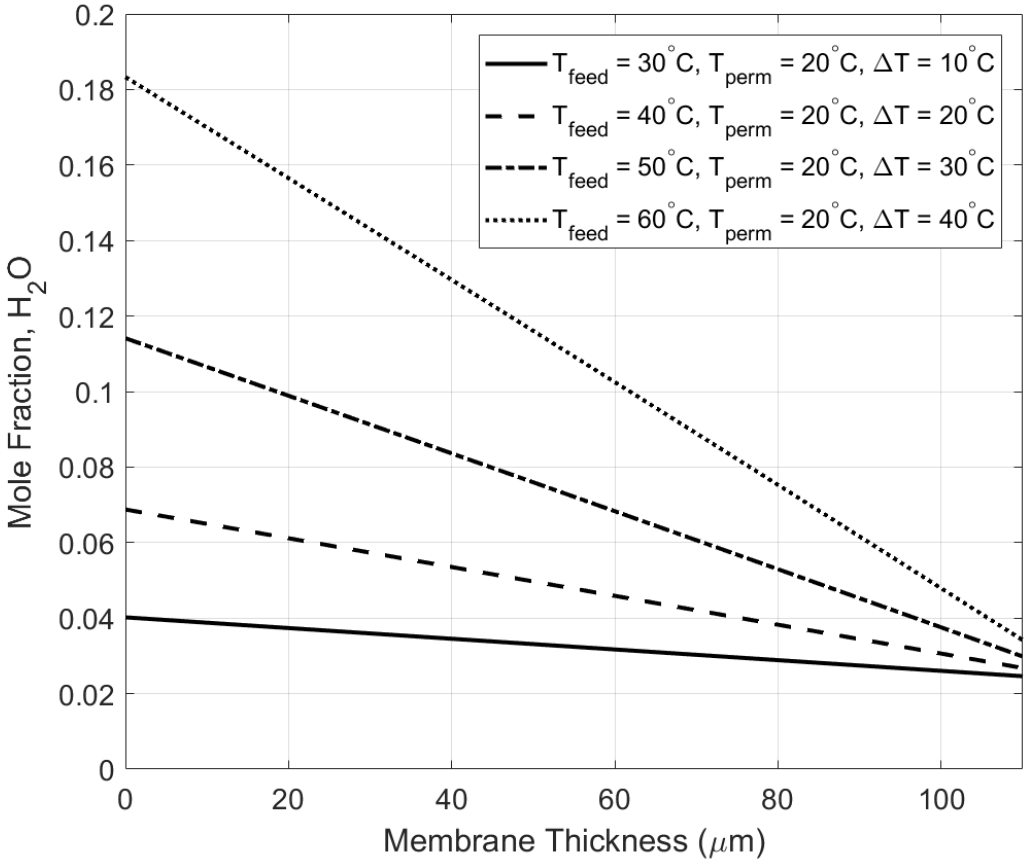

Figure 30. Water vapor mole fraction XH_2O profiles for T_{perm} = 20° C.

3.3.2. Effects of Varying Temperature Feeds

For both models, fitted tortuosity factors for the 3M 0.2 μm membrane at various temperatures were determined to explore the effects of boundary temperature on water vapor flux and tortuosity factor. Results are shown in orange in the bar plot in Figure 31. The fitted tortuosity factor value for each temperature range for the DGM (Figure 31(a)) is significantly higher than the value determined using the correlation (1.56), whereas for the Fickian diffusion model (Figure 31(b)) the tortuosity factor trends lower than the correlated value. As the temperature difference increases, the DGM fitted tortuosity factor values decrease and the Fickian diffusion model fitted values increase. The correlation used in literature for MD membranes only depends on porosity, but Figure 31 reveals that tortuosity is also dependent on the temperature for both models.

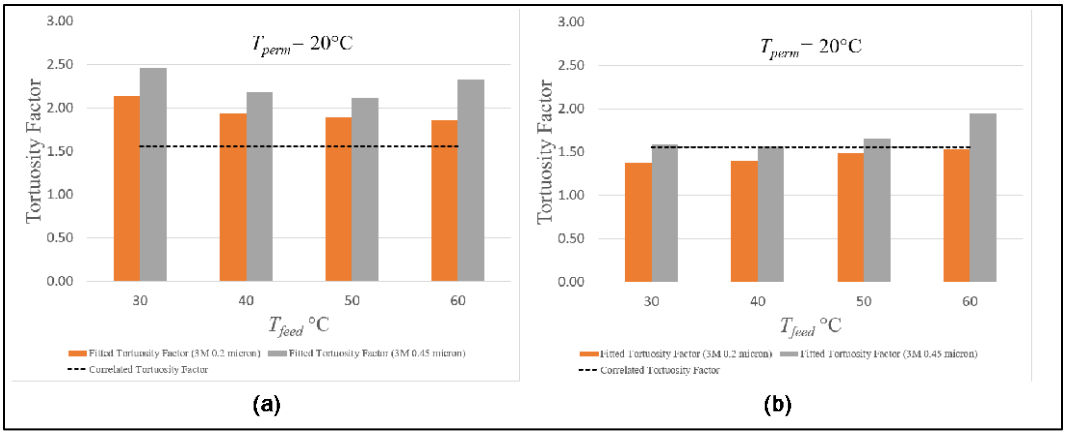

Figure 31. Fitted tortuosity factors for the (a) DGM and (b) Fickian transport models. Orange bars are for the 3M 0.2 µm membrane, and grey bars are for the 3M 0.45 µm membrane. Dashed lines show τ_{corr}.

3.3.3. Effects of Varying Microstructure on Simulation Results

A second membrane, 3M 0.45 µm, which has similar bulk parameters as the 3M 0.2 µm membrane, was simulated to predict flux and compare the fitted tortuosity factor values as a function of microstructure. Specifications for the new membrane are shown in Table 7. Between the two membranes, the only specified parameter that is different is the pore size. Ali et al. (2012) report that performance in high-porosity (> 60 percent) DCMD membranes should be largely insensitive to pore size. Therefore, it is expected that the two membranes should yield the same fitted tortuosity factor at the same operating conditions. However, the fitted tortuosity values for the 0.45 µm membrane, shown as the gray series in Figure 31, show significant differences in microstructure, and hence performance, relative to the 0.2 µm membrane.

Table 7. Membrane Specifications Provided by 3M Manufacturer

Manufacturer	Model	Base Material	Pore size	Thickness	Porosity
3M	0.45 µm	Polypropylene	0.79 µm*	110 µm	85%

*Bubble point pore diameter

As with the 0.45 µm membrane, the DGM yields fitted values that are significantly higher than the correlated value, while the Fickian diffusion model fitted values are closer to the correlated value. For both the DGM and the Fickian models, the tortuosity value increases significantly for T_{feed} = 60° C. It is unclear, at present, whether this represents an experimental outlier or if there is some fundamental phenomenon leading to poorer performance at high feed-flow temperatures. The consistency in the trend when using the Fickian diffusion

model implies that a new correlation relating tortuosity to membrane parameters and operating conditions exist and motivates additional study.

3.4. Bench-Scale CFD

We performed a parametric study of heat, mass, and momentum transport in a bench-scale MD system. We began by exploring a co-current system in which the feed temperature is varied, while holding all other operating parameters constant (Section 3.3.1). We then systematically explored the influence of feed and distillate flow rates, feed concentration, and co- versus counter-current operations. Though we also explored the effects of system length, these are not shown for brevity.

3.4.1. Co-Current Operation

Figure 32 shows the steady-state temperature field in a co-current system for which T_f =60 °C, T_d =20 °C, c_{in} =100 g/L, and U_{in} =0.124 m/s. The dimensions are those of our 10-channel experimental system. Throughout our study, we limit our feed and distillate flow rates to ensure laminar regimes. Figure 32(*a*) shows the temperature fields in the feed and permeate channels. We represent distances as the non-dimensional ratios *y/H* and *x/H*. Two different color scales are used in the distillate and feed channels to highlight the cooling of the feed and the heating of the distillate. The solid lines in panel (*b*) show the downstream variation of the membrane surface temperatures, T^f_m and T^d_m. As expected for co-current operation, the transmembrane temperature difference, ΔT_m, decreases monotonically.

The dashed lines in Figure 32(*b*) show the membrane surface temperatures $T^f_{m,Nu}$=48.06° C and $T^d_{m,Nu}$ =31.12° C, predicted by the Nusselt correlation of Hausen, (1943) as shown in Equation 30:

$$Nu = \frac{h_T D_h}{k} = 4.36 + \frac{0.036 Re_h Pr D_h/L}{1 + 0.0011 (Re_h Pr D_h/L)^{0.8}}, \quad Re_h = \frac{U_{in} D_h}{\nu}$$

Where:

h_T is the convective heat transfer coefficient

$Pr=c_p\mu/k$ is the Prandtl number

Although $T^f_{m,Nu}$ and $T^f_{m,Nu}$ provide good approximations of average membrane temperatures, they do not accurately predict the local membrane temperatures.

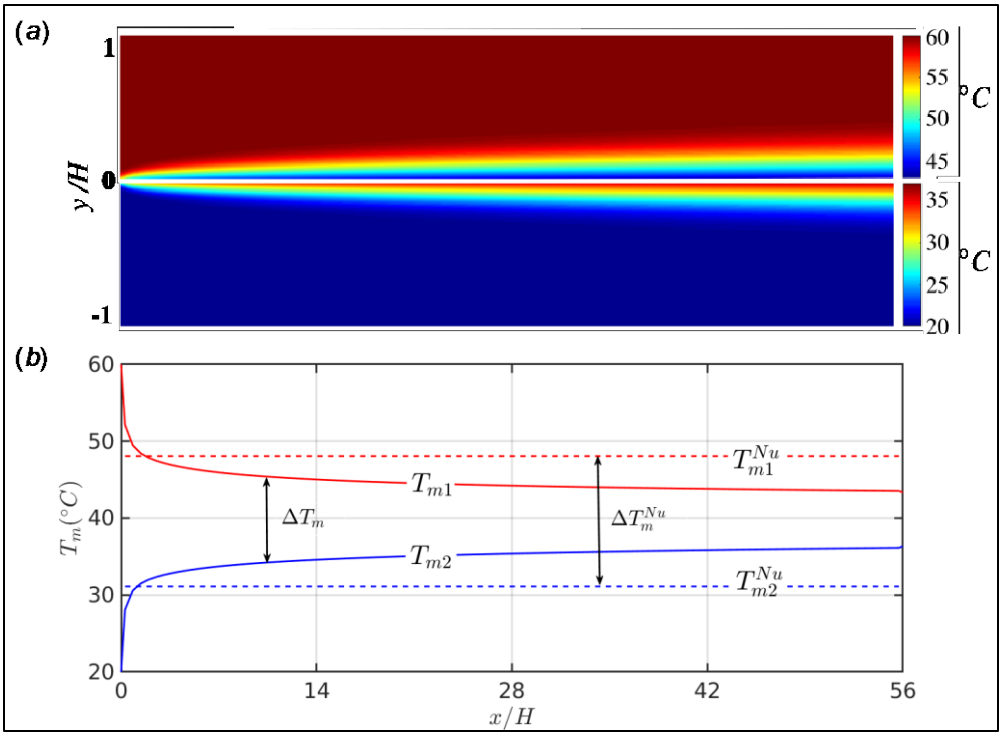

Figure 32. (a) Temperature fields for co-current operation. (b) The solid lines show the membrane temperatures evaluated from CFD. Dashed lines show the surface temperatures evaluated from a Nusselt correlation.

Figure 33(*a*) shows cross-sectional temperature profiles in the feed channel at x = L/4, L/2, 3L/4, and L. To focus on the thermal boundary layers near the membrane surface, we only show the profiles for $0 < y/H < 0.5$. As expected, the depth of the layers grows in the downstream direction. The layers are also relatively thick, covering nearly 40 percent of the channels at $x = L$. To measure the thermal boundary layer thickness in the feed channel, we define the non-dimensional temperature $\hat{T}$ and distances $\hat{x}$ and $\hat{y}$, as shown in Equation 31:

$$\hat{T} = \frac{T - T_{m1}(x)}{T_{in}^{f} - T_{m1}(x)} \qquad \hat{x} = \frac{x}{H} \qquad \hat{y} = \frac{y}{H}.$$

We then define the non-dimensional thermal boundary layer thickness $\hat{\delta}_T$ as the location where

$$\hat{T}|_{\hat{y}=\hat{\delta}_T(\hat{x})} = 0.95.$$

Figure 33(*b*) shows that the four curves in panel (*a*) collapse to a single curve when we plot $\hat{T}$ as a function of $\eta = \hat{y}/\hat{\delta}_T$,showing self-similar behavior. Figure 33(*c*) shows that $\hat{\delta}_T$ (solid line) varies with $\hat{x}$ as the power law $\hat{\delta}_T = 0.076\hat{x}^{0.36}$

(dashed line). This power law arises due to a competition between downstream heat advection and transverse heat diffusion (Probstein 1994). Though not shown, for brevity, the distillate channel satisfies an identical power-law.

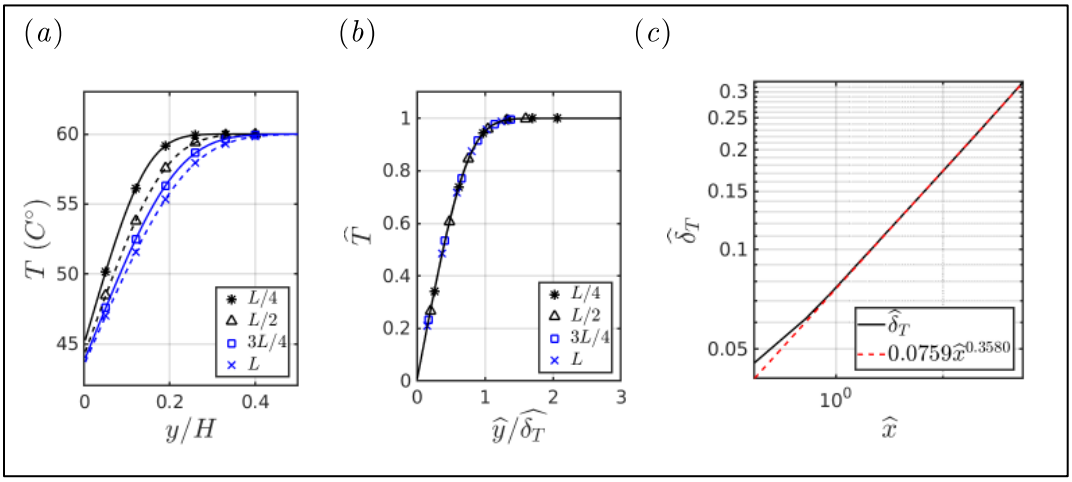

Figure 33. (a) Temperature profiles in the feed channel at x=L/4, x=L/2, x=3L/4 and x=L. (b) Self-similar behavior of temperature distributions (c) Variation of the thermal boundary layer thickness under logarithm coordinates.

Figure 34 shows the downstream variation of the transmembrane velocity, $v_m(x)$, normalized with the mean inlet velocity. The right axis shows the equivalent local permeate flux in LMH. We observe that v_m is four orders of magnitude smaller than U_{in} and decreases approximately 77 percent from 61.68 LMH at the inlet to 13.94 LMH at the outlet due. The dashed line in Figure 34 shows the average transmembrane velocity v_m^{ave} = 4.40e-5U_{in}. Thin film models of DCMD systems often neglect the downstream variation of v_m, as they apply this constant value along the entire membrane surface. Meanwhile, DCMD models based on Graetz (1882) and Leveque (1928) boundary layer solutions neglect v_m altogether.

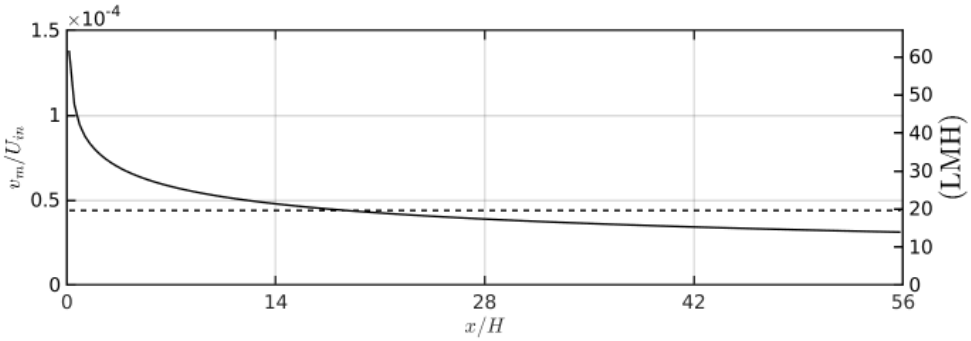

Figure 34. The solid line shows the transmembrane vapor flux for the co-current case. The dashed line shows the average flux.

Figure 35(*a*) shows the steady-state concentration field in the feed channel. Because the mass diffusivity *D* is much smaller than the thermal diffusivity α, the concentration boundary layer is much thinner than the thermal layer.

Consequently, Figure 35(*a*) only shows the concentration for $0 < y/H < 0.1$. The solid line in Figure 35(*b*) shows the downstream variation of the membrane surface concentration, $c_m(x)$. Though the permeate velocity is small, we observed a significant increase of c_m from the inlet value of 100 g/L to the outlet value around 130 g/L. As expected, c_m increased most rapidly near the inlet, where the vapor flux is a maximum. Though c_m increased dramatically over the membrane, the average feed concentration at the outlet is only c_{out} = 101.23 g/L, an increase of 1.23% from c^f_{in}. The disparity between c_m and c_{out} arises because the solute concentration occurs within a thin polarization layer. Though not shown, for brevity, we applied the same rescaling applied to the temperature boundary layer and found that the concentration layer also shows self-similarity with a $^1/_3$ power law in the x-direction.

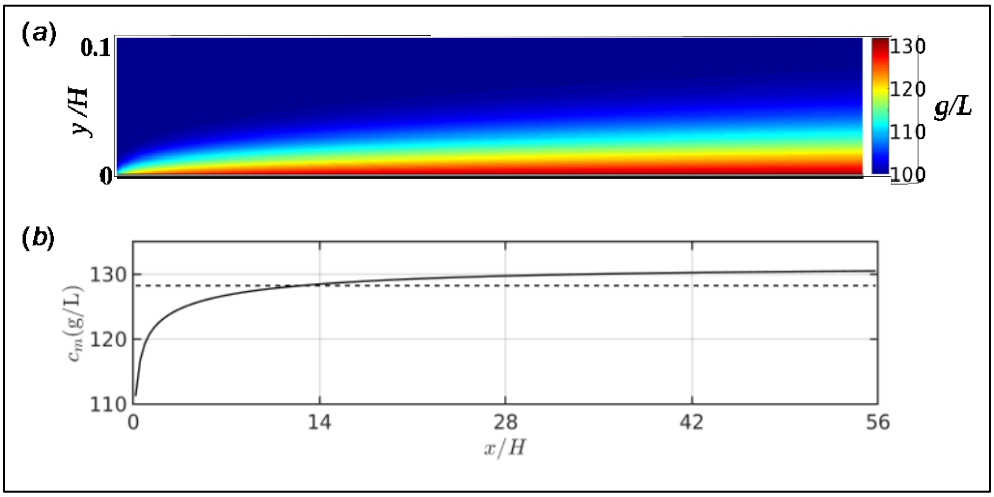

Figure 35. (a) The concentration field for 0 < y/H < 0.1. (b) The solid line shows $c_m(x)$. The dashed line shows c_m^{Sh}.

The dashed line in Figure 35(*b*) shows the uniform membrane surface concentration, c_m^{Sh}=128.27g/L, evaluated from a Sherwood number correlation developed by De and Bhattacharya (1997) as shown in Equation 32:

$$Sh = \frac{h_c D_h}{D} = 2.381 \frac{(Re_h Sc Dh/L)^{1/3}}{I} \qquad I = \int_0^\infty \exp(-\eta^3/3 - 0.42\lambda_I \eta) d\eta.$$

Where:

h_c is the convective mass transfer coefficient

$Sc=\mu/(\rho D)$ is the Schmidt number

$\lambda_I = Re_h Sc/(ReScD_h/L)^{1/3}$ is a constant.

Though c_m^{Sh} significantly overpredicts c_m in the inlet region, it accurately predicts the downstream membrane surface concentration. At the outlet, the Sherwood

relation under-predicts c_m by only 1.7 percent. However, the Sherwood relation cannot predict the downstream regions operating in supersaturated conditions.

3.4.2. Counter-Current Operation

We investigated counter-current operation by repeating the simulation of the previous section in counter-current mode. Figure 36(*a*) shows the temperature field in the channels. The solid lines in Figure 36(*b*) show that the membrane surface temperature on the feed side, T_m^f, decreases monotonically from 60 to 38.65 $^\circ$C in its downstream direction (rightward), while T_m^d increases monotonically from 20 to 43.11 $^\circ$C in its downstream direction (leftward). As expected, the surface temperatures vary most rapidly at the inlets and outlets. The dashed lines show the uniform surface temperatures, $T^f_{m,Nu}$=48.00 ◦C and $T^d_{m,Nu}$=31.17 ◦C, predicted by the Nusselt correlation of Hausen (1943).

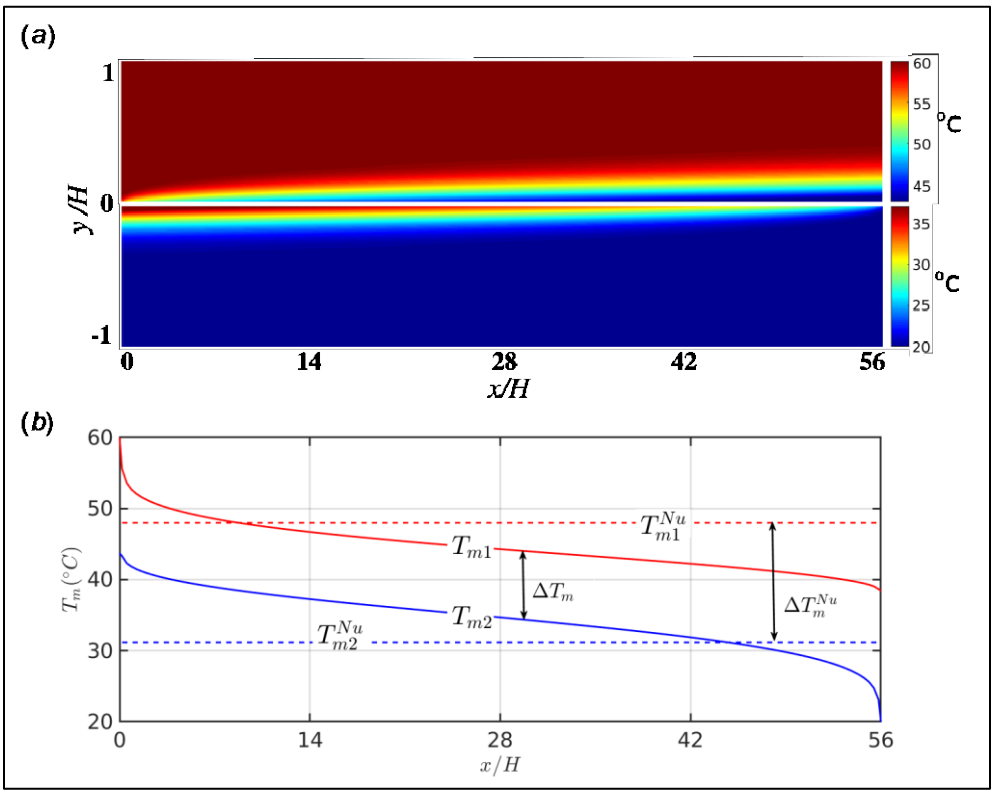

Figure 36. (a) Temperature field for counter-current arrangement. (b) Solid lines show the downstream variation of membrane temperatures. Dashed lines show the membrane surface temperature evaluated from a Nusselt correlation.

Figure 37 shows that the temperature difference $\Delta T_m(x)$ (panel *a*) and vapor flux $v_m(x)$ (solid line, panel *b*) vary non-monotonically in a counter-current system. Perhaps unexpectedly, the temperature difference is maximized at the feed outlet, while the vapor flux is maximized at the inlet. This occurs because the saturation pressure P^{sat} varies non-linearly with temperature, such that dP^{sat}/dT increases

with temperature. In addition, vapor pressure reduction due to concentration polarization is maximized at the outlet. These compounding phenomena also cause the vapor flux to be minimized near $x/L = 3/4$. For comparison, the dashed line in panel (*b*) shows the vapor flux in a co-current system. Overall, the counter-current operation produces a net permeate flux of 20.54 LMH, compared to 19.62 LMH for co-current operation.

Figure 37(*c*) shows the surface concentration $c_m(x)$ for co-current (dashed line) and counter-current (solid line) operation. Though counter-current operation produces only a small increase in net permeate flux, it produces a roughly 40 percent increase in membrane concentration, compared to approximately 30 percent for co-current operation. Throughout our study, we continued to find that counter-current operation produced only a modest increase in permeate flux but significantly increased concentration polarization. The dashed line in Figure 37(*c*) shows the surface concentration $c_m^{sh} = 129.54$ g/L produced by the Sherwood correlation of De and Bhattacharya (1997). Though c_m^{sh} showed promising agreement for co-current operation, it over- and under-predicts c_m near the inlet and outlet, respectively, of the counter-current system.

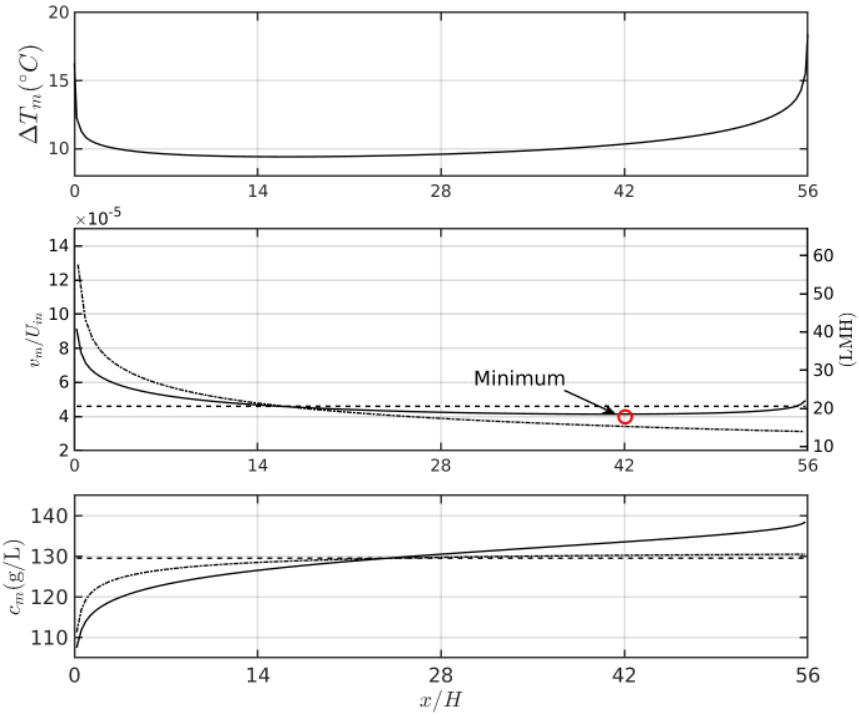

Figure 37. (a) Downstream variation of ΔT_m. (b) The solid and dash-dotted lines show $v_m(x)$ for co- and counter-current cases, respectively. The dashed line shows the average vapor flux for the counter-current case (c). The solid and dash-dotted lines show the downstream variation of c_m for co- and counter-current cases, respectively. The dashed line shows c_m^{sh} for the counter-current case.

3.4.3. Feed Temperature Effects

To investigate the effects of feed and distillate inlet temperatures, we simulated co- and counter-current operations for feed temperatures $30 \leq T_f \leq 90°$ C and distillate temperatures $20 \leq T_d \leq 80°$ C. All other parameters were held in constant as in previous sections. For brevity, we only report here the results for constant distillate temperature T_d=20° C.

Figure 38(a) shows the variation of the average vapor flux, v_m^{ave}, with increasing feed inlet temperature. Panel (b) shows the corresponding variation of the maximum concentration c_{max} normalized with C_{in}. In all cases, counter-current operation (solid lines) produced only marginally more flux than co-current operation (dashed lines), but significantly more concentration polarization. In practice, DCMD systems recycle heat from the feed and distillate outflows to preheat the feed.

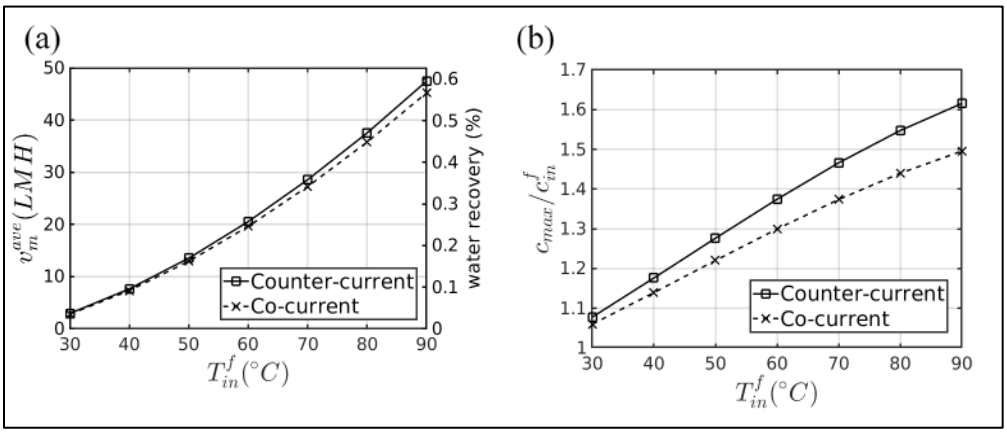

Figure 38. (a) Variation of (a) the average vapor flux v_m^{ave} and (b) the maximum concentration c_{max} with varying feed temperature. The right axis of (a) shows the corresponding water recovery.

As sketched in Figure 39, we investigated the effects of heat recycling by considering a system in which two heat exchangers preheat the feed using waste heat from the outlet flows. After preheating, a heater brings the feed to the desired inlet temperature. We computed the Gained Output Ratio (GOR) where Q_{in} is the energy input to the heater and Q_v is the net evaporative heat transfer. Note that GOR can be greater than unity, because most of the energy used to heat the feed inlet flow is from the feed and distillate outlets.

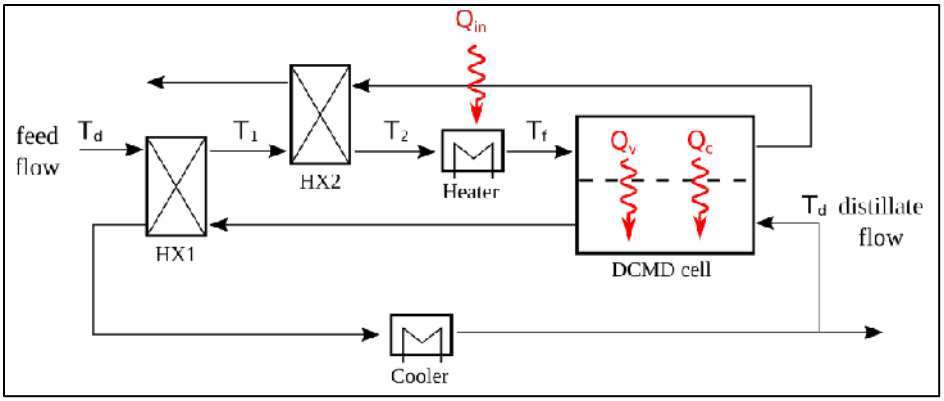

Figure 39. Sketch demonstrating heat recovery from the feed and distillate outlet flows.

To estimate the GOR, we used plate heat exchangers manufactured by WCR Incorporated (Model WCR-A102). Using the manufacturer-provided heat transfer coefficient, we use the Effectiveness-NTU method[48] to compute Q_{in} as shown in Equation 33:

$$GOR = \frac{Q_v}{Q_{in}} = \frac{\int_0^L j_v \lambda dx}{Q_{in}}$$

Figure 40 shows the variation of GOR with T_f. The GOR increases monotonically with feed temperature increases because the net evaporative heat transfer Q_v increases more rapidly with T_f than Qin, as illustrated in panel (b). We also observed that co-current operation always produces a greater GOR than counter-current.

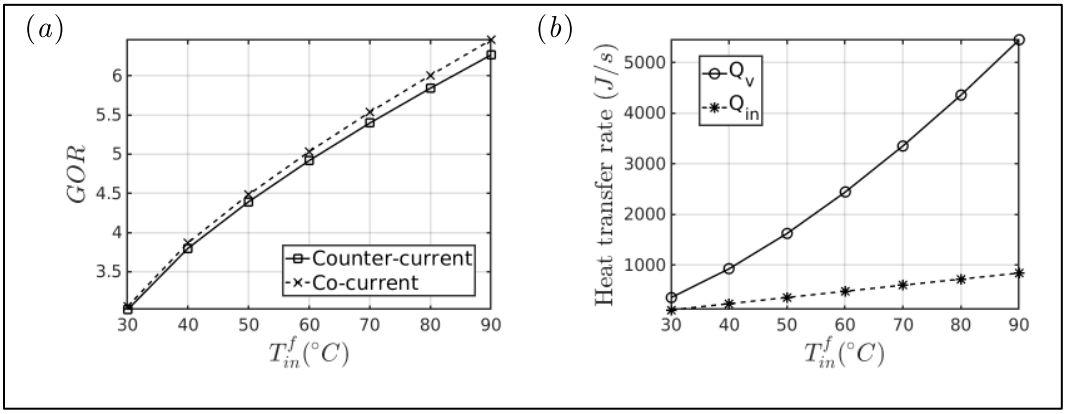

Figure 40. (a) Variation of GOR with Tf. (b) Variation of Qv and Qin for co-current operation.

3.4.4. Feed Concentration

To investigate the effects of feed concentration, we simulated co- and counter-current operations for feed concentrations $0 < C_{in} < 300$ g/L in increments of 50 g/L. All other parameters were fixed as described in Sections 3.3.1 and 3.3.2.

Figure 41 shows the variation of v_m^{ave} and c_{max} with varying feed concentration. For both configurations, the average vapor flux decreases almost linearly with increasing feed concentration due to the decrease in vapor pressure on the feed surface of the membrane. For counter-current operation, for example, the net transmembrane flux decreases over 50% from 24.58 LMH at C_{in}=0 g/L to 11.97 LMH at C_{in}=300 g/L. Panel (b) shows that the decrease in the transmembrane flux causes a decrease in concentration polarization.

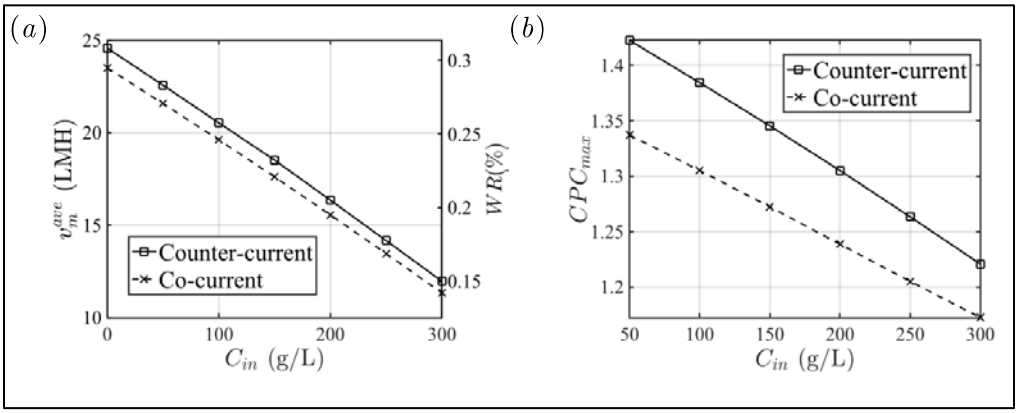

Figure 41. Variation of v_m^{ave} (panel a) and c_{max} (panel b) with varying feed concentration.

For counter-current operation, c_{max}/C_{in} decreases from 1.42 at C_{in}=50 g/L to 1.22 at C_{in} =300 g/L. The latter value corresponds to 366 g/L, which exceeds the saturation value C_{sat}=364 g/L, computed at the feed outlet membrane temperature T=41.18° C. Thus, we expect mineral scaling to occur on the membrane near the feed outlet. For both co- and counter-current operations, Figure 42 shows that the decrease in permeate flux causes a more than 25 percent drop in GOR.

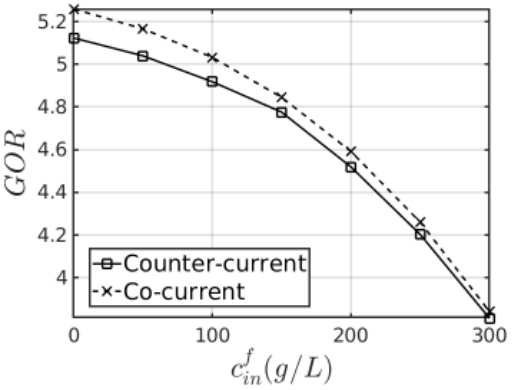

Figure 42. Variation of GOR with C_{in}.

3.4.5. Feed Velocity

To investigate the effects of inlet velocity, we simulated co- and counter-current operations for $0.041 \leq U_{in} \leq 0.248$ m/s, corresponding to the laminar Reynolds numbers $175 < Re_f < 1048$ and $131 < Re_d < 783$. All other parameters are set as described in Sections 3.1 and 3.2. Figure 43 shows the variation of v_m^{ave} with varying inlet velocity. For both configurations, v_m^{ave} increases significantly (roughly 40%) with U_{in}. Panel (b) shows, however, that the single-pass water

recovery decreases with inlet velocity. This is because the inlet flow rate increases faster than v_m^{ave}.

The increase in water flux with feed velocity occurs due to a decrease in both temperature and concentration polarization, as demonstrated in Figure 44. The GOR, however, decreases roughly 80 percent, as shown in Figure 45, because the increased flow rate requires an increase in Q_{in}.

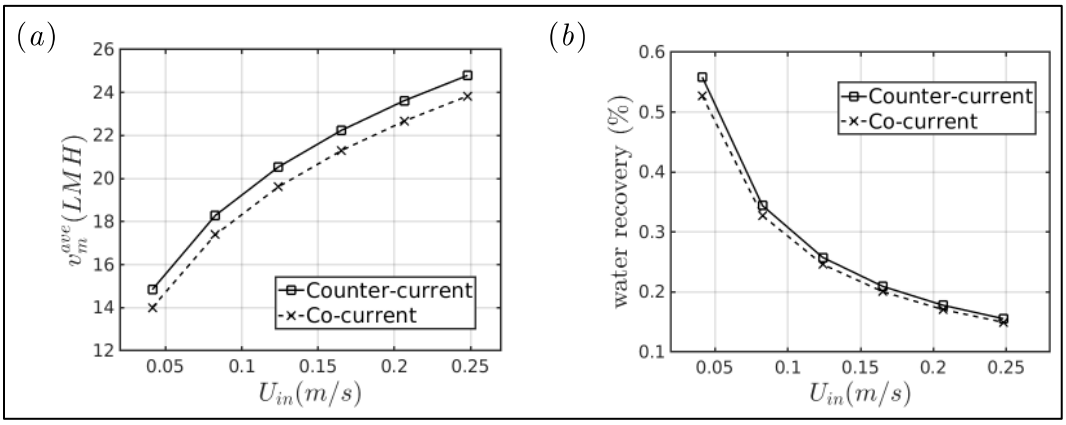

Figure 43. (a) Variation of net vapor flux for co-current (dashed) and counter-current (solid) with varying inlet velocity. (b) Variation of water recovery with varying inlet velocity.

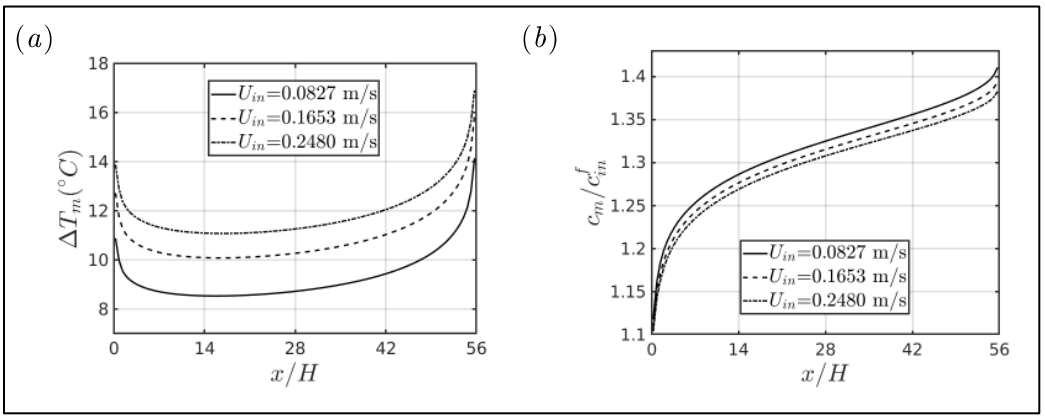

Figure 44. (a) ΔT_m and (b) c_m for varying inlet velocity, counter-current operation.

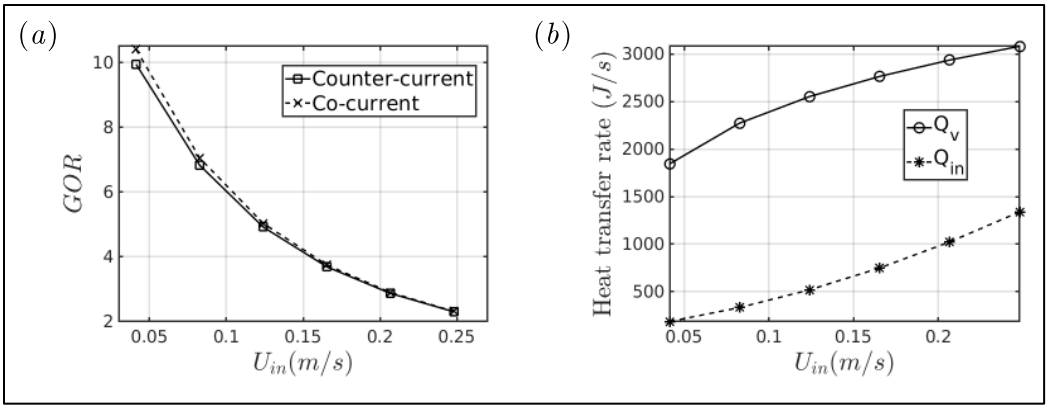

Figure 45. (a) Variation of GOR with varying U_{in}. (b) Corresponding variation of Qv and Q_{in} in a counter current system.

4. Conclusions

4.1. Conclusions

In this study, we compared the bench-scale performance of 17 potential DCMD membranes from six vendors. The membranes covered every active layer material commonly considered for DCMD, and encompassed a wide range of porosities, thicknesses, and supporting layers. The large spread in membrane properties yielded a large spread in vapor flux, thermal efficiency, rejection, and contact angle. Overall, we observed that membranes without support layers, higher porosities, and smaller thicknesses tended to have greater vapor flux; however, there were important exceptions, such that no clear trend appeared to consistently explain why one membrane outperforms another. Thus motivated, we selected five membranes for pore-scale analysis using FIB-SEM.

To understand the fundamental physics behind these results, our study undertook parallel exploration of the following:

1. Pore-scale phenomena relating trans-membrane fluxes to membrane microstructure, and
2. Impact of fluid dynamics on concentration and temperature polarization in feed and permeate flow channels.

In this study, we demonstrated the first-ever use of FIB-SEM for microstructural characterization of MD membranes. A key difficulty in performing this analysis relates to sample preparation, particularly providing significant electrical conductivity and electron microscope contrast between the epoxy used to fill membrane pores and the solid membrane polymer. We demonstrated protocols for membrane infiltration via staining membranes with heavy-metal salts and by incorporating conductive polymers into the epoxy. While the resulting FIB-SEM

images do not fully resolve the membrane microstructure (in particular, the thin, nm-scale fibers connecting larger clusters of fibers are not resolved via the FIB-SEM images), these images provide an initial view into the complex membrane microstructures and demonstrate the bimodal nature of the polymer structure, which consists of finer (roughly 40 to 50 nm thick) fibers, which connect larger bundles. Moreover, with the sample preparation protocols established in this study, future work can focus on optimizing the FIB-SEM imaging conditions for fully resolved 3D microstructures.

Detailed 1D pore-scale transport models were validated against these bench-scale DCMD experiments to understand the influence of membrane microstructure on membrane performance and its coupling with operating conditions (such as feed and permeate temperatures).

Fitting against the experimental data here leads to several important conclusions:

1) The tortuosity factor plays a critical role in describing the impact of microstructure on MD fluxes.
2) Moreover, the fitted tortuosity factors are influenced by the microstructure and also vary with operating conditions such as temperature.
3) Finally, results show that typical theories which underpin porous media transport models are not directly transferrable to MD.

In particular, while the commonly used Knudsen number would predict that molecular and Knudsen diffusion both play important roles in pore-scale MD transport processes, results here suggest that the effects of Knudsen diffusion are rather limited. Instead, results suggest that simpler Fickian models of molecular diffusion and pressure-driven Darcy flow more accurately predict trans-membrane fluxes.

We developed an in-house CFD code that simulates heat and mass transport in 2D DCMD systems. The code was developed using well-established models for transmembrane heat and mass transport and was validated against dedicated experiments in a bench-scale DCMD system. The code was then used to perform a comprehensive parametric study of temperature polarization, concentration polarization, and system level efficiency as a function of co- vs. counter-current operation, operating temperature, feed concentration, flow rate, and system length.

Our CFD study showed that common Nusselt and Sherwood number relationships do not accurately predict temperature and concentration polarization. Moreover, though DCMD systems have small vapor fluxes, they produce significant concentration polarization. Compounding effects of temperature and concentration polarization can also have counter-intuitive effects on local transmembrane vapor flux, such that the maximum vapor flux does not occur

where the transmembrane temperature is maximized. Furthermore, counter-current operation was found to only produce a marginal increase in net vapor production but has a significantly greater concentration polarization. As a result, co-current systems were found to have a higher Gained Output Ratio than counter-current systems.

4.2. Recommended Next Steps

These results provide important insights in their own right, but also inspire further research in the areas of pore-scale phenomena and CFD modeling of flow channel temperature, concentration, and velocity profiles.

Further study is required for pore-scale phenomena to optimize using FIB-SEM for membrane microstructural characterization. This study successfully demonstrated infiltration procedures to enable FIB-SEM characterization, but now the FIB-SEM procedure itself requires fine-tuning. Identifying optimal beam current and other settings would enable FIB-SEM reconstructions that preserve the fully 3D microstructure of the membranes, including the thinner fibers that were not resolved in the current study.

Following successful 3D imaging of the membrane microstructure, the detailed CFD on the reconstructed microstructures can proceed, using commercial software such as FLUENT. These simulations can then be used as a numerical experiment to better understand heat and mass transport mechanisms in the MD membranes.

The 1D simulation results herein suggest that the tortuosity factor τ, commonly used in such simulations, depends on more than just membrane microstructure. The dependence of the fitted τ values on the feed and permeate temperatures, for example, suggest that the tortuosity is compensating for transport phenomena current not included in standard models. Additional work is required to identify and incorporate additional temperature-dependent phenomena in the membrane flux equations. Furthermore, the current 1D modeling tools need to be extended to 2D in order to properly validate against the bench-scale experiments.

We identified numerous avenues for future CFD work, and several of these studies are now underway:

- First, though the transmembrane heat and mass transport models incorporated in our CFD were relatively simple and well established, determining the appropriate vapor permeability and thermal conductivity for these models was not straightforward. Eventually, we decided to use published estimates for the thermal conductivity, and then fit the vapor permeability by comparing our simulations to experiments. While this produced promising agreement, we could just as well have used published

values of permeability and then fit the thermal conductivity. These are precisely the issues that motivated our pore-scale study.

- Second, though not included in this report, we have also performed preliminary simulations of heat and mass transport in 3D DCMD systems. These simulations show that temperature and concentration polarization vary significantly in the transverse direction, such that 3D effects are important. We are currently optimizing our 3D code for efficiency and plan to perform a parametric study of 3D polarization in DCMD systems.
- Third, our bench-scale experiments showed that feed and distillate spacers play a key role in heat and mass transport in DCMD systems. We developed a preliminary code to simulate simple 2D spacers, and these confirmed that spacers play an important role in mineral scaling. We have recently been awarded funding from the NSF and the Colorado Office of Economic Development and International Trade to explore these issues in both DCMD and RO systems.

References

Ali, M. I., Summers, E. K., Arafat, H. A., and V, J. H. L., 2012. "Effects of membrane properties on water production cost in small scale membrane distillation systems," *Desalination*, vol. 306, Nov. 2012, pp. 60–71.

Alves, V. D., and Coelhoso, I. M., 2004."Effect of membrane characteristics on mass and heat transfer in the osmotic evaporation process," *Journal of Membrane Science*, vol. 228, pp. 159–167.

Andrjesdóttir, Ó., Ong, C. L., Nabavi, M., Paredes, S., Khalil, A. S. G., Michel, B., and Poulikakos, D., 2003. "An experimentally optimized model for heat and mass transfer in direct contact membrane distillation," *International Journal of Heat and Mass Transfer*, vol. 66, Nov. 2013, pp. 855–867.

Bouchrit, R., Boubakri, A., Hafiane, A., and Bouguecha, A. A.-T., 2015. "Direct contact membrane distillation: Capability to treat hyper-saline solution," *Desalination*, vol. 376, 2015, pp. 117–129.

Bush, J. A., Vanneste, J., Cath, T., 2016. "Membrane distillation for concentration of hypersaline brines from the great salt lake: Effects of scaling and fouling on performance, efficiency, and salt rejection," *Separation and Purification Technology*, vol. 170, pp. 78–91.

Choi, H. and Moin, P., 1994. "Effects of the computational time step on numerical solutions of turbulent flow," *Journal of Computational Physics*, vol. 113, pp. 1–4.

Cooper, S. J., Bertei, A., Shearing, P. R., Kilner, J. A., and Brandon, N. P., 2016. "TauFactor: An open-source application for calculating tortuosity factors from tomographic data," *SoftwareX*, vol. 5, pp. 203–210.

De, S. and Bhattacharya, P. K., 1997. "Prediction of mass-transfer coefficient with suction in the applications of reverse osmosis and ultrafiltration," *Journal of Membrane Science*, vol. 128, pp. 119–131.

DeCaluwe, S. C. Gilleon, S., "1D membrane distillation modeling tool." https://github.com/coresresearch/membrane_distillation.git. Accessed June 3, 2019.

Ferziger, J. H. and Peric, M., 2002. *Computational Methods for Fluid Dynamics*, Berlin: Springer.

Field, R. W., Wu, H. Y., and Wu, J. J., 2013. "Multiscale Modeling of Membrane Distillation: Some Theoretical Considerations," *Industrial & Engineering Chemistry Research*, vol. 52, July 2013, pp. 8822–8828.

Gao, F., Chen, X., Yu, G., and Asumana, C., 2011. “Compressible gases transport through porous membrane: A modified dusty gas model,” *Journal of Membrane Science*, vol. 379, September 2011, pp. 200–206.

Graetz, L. 1882. Ueber die Wärmeleitungsfähigkeit von Flüssigkeiten. *Annalen der Physik*. 254: 79.

Hausen, H., 1943. “Darstellung dses warmeuberganges in rohren durch verallgemeinerte potenzbeziehungen,” *Z. VDI Beih. Verfahrenstech*, vol. 4, pp. 91–98.

Harned, H. S. and Hildreth, J. C. L., 1951. “The differential difussion coefficients of lithium and sodium chlorides in dilute aqueous solution at 25,” *Journal of the American Chemical Society*, vol. 73, pp. 650–652.

Hickenbottom, K. L. and Cath, T. Y., 2014. “Sustainable operation of membrane distillation for enhancement of mineral recovery from hypersaline solutions,” *Journal of Membrane Science*, vol. 454, pp. 426–435.

Hitsov, I., Maere, T., De Sitter, K., Dotremont, C., and Nopens, I., 2015 “Modelling approaches in membrane distillation: A critical review,” *Separation and Purification Technology*, vol. 142, March 2015, pp. 48–64.

Khayet, M., 2011. “Membranes and theoretical modeling of membrane distillation: A review,” *Advances in Colloid and Interface Science*, vol. 164, pp. 56–88.

Khayet, M., Imdakm, A. O., and Matsuura, T., 2010. “Monte Carlo simulation and experimental heat and mass transfer in direct contact membrane distillation,” *International Journal of Heat and Mass Transfer*, vol. 53, March 2010, pp. 1249–1259.

Kizilyaprak, C., Longo, G., Daraspe, J., and Humbel, B. M., 2015. “Investigation of resins suitable for the preparation of biological sample for 3-D electron microscopy,” *Journal of Structural Biology*, vol. 189, pp. 135–146.

Knott, G., Rosset, S., and Cantoni, M., 2011. “Focussed Ion Beam Milling and Scanning Electron Microscopy of Brain Tissue,” *Journal of Visualized Experiments*, pp. 3–6.

Kremer, A., Lippens, S., Bartunkova, S., Asselbergh, B., et al. 2015. “Developing 3D SEM in a broad biological context,” *Journal of Microscopy*, vol. 259, pp. 80–96.

Leveque, M. A., 1928, “Les lois la transmission de chaleur par convection,” *Anales des Mines*, vol. 13.

Lešer, V., Drobne, D., Pipan, Z.˘, Milani, M., and Tatti, F., 2009. "Comparison of different reparation methods of biological samples for FIB milling and SEM investigation," *Journal of Microscopy*, vol. 233, pp. 309–319.

Lawson, K. W. and Lloyd, D. R., 1997. "Membrane distillation," *Journal of Membrane Science*, vol. 124, pp. 1–25.

Mackie, J. S. and Meares, P., 1955. "The diffusion of electrolytes in a cation-exchange resin membrane I. Theoretical," *Proceedings of the Royal Society of London. Series A. Mathematical and Physical Sciences*, vol. 232, November 1955, p. 498 LP--509.

Narayan, K. and Subramaniam, S., 2015. "Focused ion beams in biology," *Nature Methods*, vol. 12, pp. 1021–1031.

Pacheco, F. A., Pinnau, I., Reinhard, M., and Leckie, J. O., 2010. "Characterization of isolated polyamide thin films of RO and NF membranes using novel TEM techniques," *Journal of Membrane Science*, vol. 358, pp. 51–59.

Probstein, R. F., 1994. *Physicochemical Hydrodynamics*, John Wiley & Sons.

Ramirez, M. L. V. and Castro, C. A. N. de, 1994. "Thermal conductivity of aqueous sodium chloride solutions," *Journal of Chemical Engineering Data*, vol. 39, pp. 186-190.

Rao, G., Hiibel, S. R., and Childress, A. E., 2014. "Simplified flux prediction in direct-contact membrane distillation using a membrane structural parameter," *Desalination*, vol. 351, October 2014, pp. 151–162.

Ruwin, P., 2013. "EM Sample Preparation," *Leica Microsystems*, pp. 3–16.

Sani, R. L. and Gresho, P. M.,1994. "Resume and remarks on the open boundary condition minisymposium," *International Journal for Numerical Methods in Fluids*, vol. 18, pp. 983-1008.

Schofield, R. W., Fane, A. G., and Fell, C. J. D., 1987. "Heat and mass transfer in membrane distillation," *Journal of Membrane Science*, vol. 33, pp. 299–313.

Sears, K., Dumée, L., Schütz, J., She, M., Huynh, C., Hawkins, S., Duke, M., and Gray, S., 2010. "Recent developments in carbon nanotube membranes for water purification and gas separation," *Materials*, vol. 3, pp. 127–149.

Seligman, A. M., Wasserkrug, H. L., and Hanker, J. S., 1966."A new staining method (OTO) for enhancing contrast of lipid--containing membranes and droplets in osmium tetroxide--fixed tissue with osmiophilic

thiocarbohydrazide(TCH).," *Journal of Cell Biology*, vol. 30, pp. 424–432.

Sheidaei, A., Baniassadi, M., Banu, M., Askeland, P., Pahlavanpour, M., Kuuttila, N., Pourboghrat, F., Drzal, L. T., and Garmestani, H., 2013. "3-D microstructure reconstruction of polymer nano-composite using FIB–SEM and statistical correlation function," *Composites Science and Technology*, vol. 80, May 2013, pp. 47–54.

Shirazi, M. M. A., Kargari, A., Ismail, A. F., and Matsuura, T., 2016. "Computational Fluid Dynamic (CFD) opportunities applied to the membrane distillation process: State-of-the-art and perspectives," *Desalination*, vol. 377, Jan. 2016, pp. 73–90.

Sirkar, K. K. and Li, B., 2003. "Novel membrane and device for direct contact membrane distillation-based desalination process: Phase II," *DWPR Program Report No. 97*.

Sirkar, K. K. and Qin, Y., 2001."Novel membrane and device for direct contact membrane distillation based desalination process," *DWPR Program Report No. 87*.

Sirkar, K. K., and Song, L., 2009. "Pilot-scale studies for direct contact membrane distillation-based desalination process," *DWPR Program Report No. 134*.

Smith, J. R., Chen, A., Gostovic, D., Hickey, D., Kundinger, D., Duncan, K. L., DeHoff, R. T., Jones, K. S., and Wachsman, E. D., 2009. "Evaluation of the relationship between cathode microstructure and electrochemical behavior for SOFCs," *Solid State Ionics*, vol. 180, February 2009, pp. 90–98.

Srisurichan, S., Jiraratananon, R., and Fane, A. G., 2006. "Mass transfer mechanisms and transport resistances in direct contact membrane distillation process," *Journal of Membrane Science*, vol. 277, pp. 186–194.

Vanneste, J., J. A. Bush, K. L. Hickenbottom, C. A. Marks, D. Jassby, C. S. Turchid, T. Y. C., 2018. "Novel thermal efficiency-based model for determination of thermal conductivity of membrane distillation membranes," *Journal of Membrane Science*, vol. 548, pp. 298–308.

Wiedemann, H. Goldin, A., Barnett, G., Zhu, S., and Kee, R., 2013."Effects of three-dimensional cathode microstructure on the performance of lithium-ion battery cathodes," *Electrochimica Acta*, vol. 88, pp. 580–588.

Yu, H., Yang, X., Wang, R., and Fane, A. G., 2011. "Numerical simulation of heat and mass transfer in direct membrane distillation in a

hollow fiber module with laminar flow," *Journal of Membrane Science*, vol. 384, November 2011, pp. 107–116.